Synergistic Regulation of S-Vacancy of MoS$_2$-Based Materials for Highly Efficient Electrocatalytic Hydrogen Evolution

Xiao-Yun Li[1], Shao-Ju Zhu[2], Yi-Long Wang[3]*, Tian Lian[2], Xiao-yu Yang[2], Cui-Fang Ye[4], Yu Li[2], Bao-Lian Su[2] and Li-Hua Chen[2]*

[1]State Key Laboratory of Silicate Materials for Architectures, Wuhan University of Technology, Wuhan, China, [2]State Key Laboratory of Advanced Technology for Materials Synthesis and Processing, Wuhan University of Technology, Wuhan, China, [3]School of Chemistry, Chemical Engineering and Life Science, Wuhan University of Technology, Wuhan, China, [4]Department of Histology and Embryology, Tongji Medical College, Huazhong University of Science and Technology, Wuhan, China

Low or excessively high concentration of S-vacancy ($C_{\text{S-vacancy}}$) is disadvantageous for the hydrogen evolution reaction (HER) activity of MoS$_2$-based materials. Additionally, alkaline water electrolysis is most likely to be utilized in the industry. Consequently, it is of great importance for fine-tuning $C_{\text{S-vacancy}}$ to significantly improve alkaline hydrogen evolution. Herein, we have developed a one-step Ru doping coupled to compositing with CoS$_2$ strategy to precisely regulate $C_{\text{S-vacancy}}$ of MoS$_2$-based materials for highly efficient HER. In our strategy, Ru doping favors the heterogeneous nucleation and growth of CoS$_2$, which leads to a high crystallinity of Ru-doped CoS$_2$ (Ru-CoS$_2$) and rich heterogeneous interfaces between Ru-CoS$_2$ and Ru-doped MoS$_{2-x}$ (Ru-MoS$_{2-x}$). This facilitates the electron transfer from Ru-CoS$_2$ to Ru-MoS$_{2-x}$, thereby increasing $C_{\text{S-vacancy}}$ of MoS$_2$-based materials. Additionally, the electron injection effect increases gradually with an increase in the mass of Co precursor (m_{Co}), which implies more S^{2-} leaching from MoS$_2$ at higher m_{Co}. Subsequently, $C_{\text{S-vacancy}}$ of the as-synthesized samples is precisely regulated by the synergistic engineering of Ru doping and compositing with CoS$_2$. At $C_{\text{S-vacancy}}$ = 17.1%, a balance between the intrinsic activity and the number of exposed Mo atoms (EMAs) to boost highly active EMAs should be realized. Therefore, the typical samples demonstrate excellent alkaline HER activity, such as a low overpotential of 170 mV at 100 mA cm^{-2} and a TOF of 4.29 s^{-1} at -0.2 V. Our results show promise for important applications in the fields of electrocatalysis or energy conversion.

Keywords: S-vacancy of MoS$_2$, heterogeneous interfaces, exposed Mo atoms, electrocatalysis, hydrogen evolution reaction
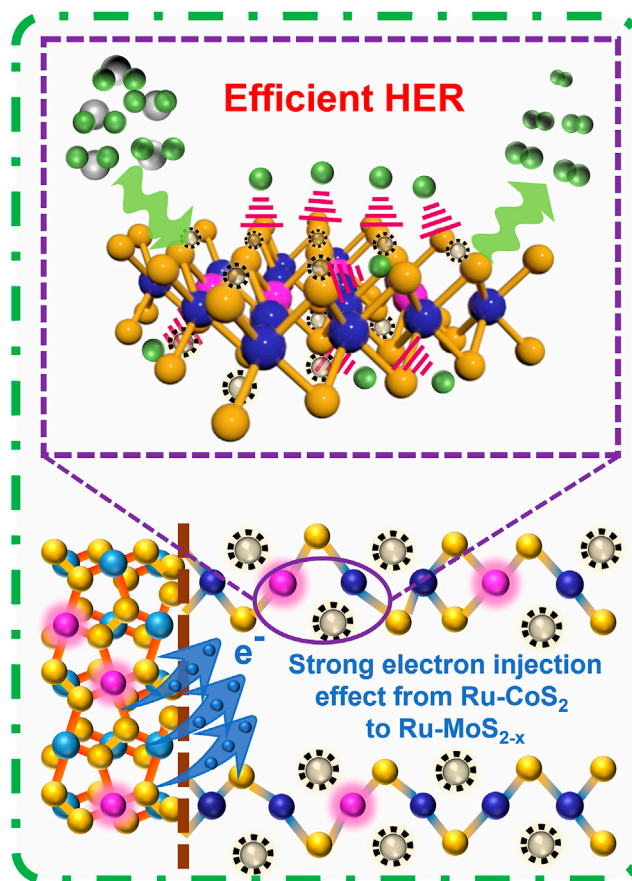
Graphical Abstract |

INTRODUCTION

The rapid development of the economy has made the fast consumption of fossil energy, resulting in the energy crisis and severe environmental pollution (Xie et al., 2013b; Xu et al., 2017; Jiang et al., 2022). Hydrogen energy, as one of the clean and renewable energies, has received extensive attention around the world (Huang et al., 2019; Venkateshwaran and Senthil Kumar, 2019; Zhu et al., 2019; Wang F. et al., 2020). Electrocatalytic water splitting (Lin et al., 2017; Lin et al., 2019; Djara et al., 2020; Liu L. et al., 2022) is regarded as an eco-friendly technology for hydrogen (H_2) production. So far, platinum-based materials are still the best electrocatalysts for acidic water electrolysis (Chen et al., 2020). Nevertheless, the high cost and low abundance seriously restrict the wide applications of such precious metals (Li et al., 2011; Qi et al., 2019; Jing et al., 2020). On the other hand, alkaline water electrolysis is most likely to be utilized in the industry, owing to the unrestricted reactant availability, desirable safety, and satisfactory output (Yin et al., 2015). However, the sluggish dynamics of hydrogen evolution reaction (HER) in alkaline environments results in excessive energy consumption (Yin et al., 2015). Therefore, it is of

great significance for the development of highly efficient and low-cost electrocatalysts to overcome energy barriers for accelerating kinetics and to decrease overpotential during the hydrogen evolution reaction (HER) process.

It is well known that molybdenum disulfide (MoS_2) can be designed as an alternative to Pt due to the excellent H* adsorption–desorption properties, special layered structures, good stability, and low cost (Hinnemann et al., 2005; Deng et al., 2017; Wang Y. et al., 2019; Gao et al., 2020). However, the pristine 2H-MoS_2 tends to aggregate under van der Waals forces, resulting in poor edge active sites (Kibsgaard et al., 2012; Wang et al., 2017; Wang et al., 2021b). More importantly, there remain a lot of active sites from the vast basal planes of such MoS_2 to be developed (Kibsgaard et al., 2012; Wang et al., 2017; Wang et al., 2021b). To address these drawbacks, defect-rich, double-gyroid, and amorphous structures have been introduced into such MoS_2 nanosheets to increase the unsaturated sulfur atoms as active sites for HER (Kibsgaard et al., 2012; Xie et al., 2013a; Liu et al., 2018). Doping transition metals (TMs) into MoS_2 is another important method for the advancement of electrocatalysis. This is because doping TMs not only increases the number of unsaturated sulfur atoms but also regulates the adsorption free
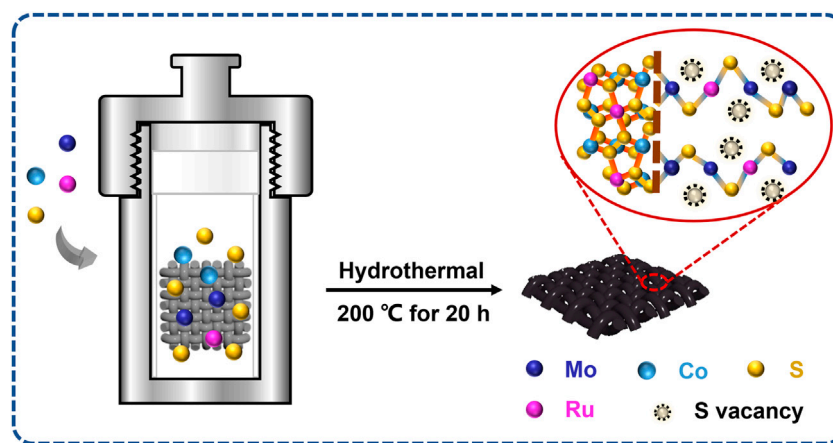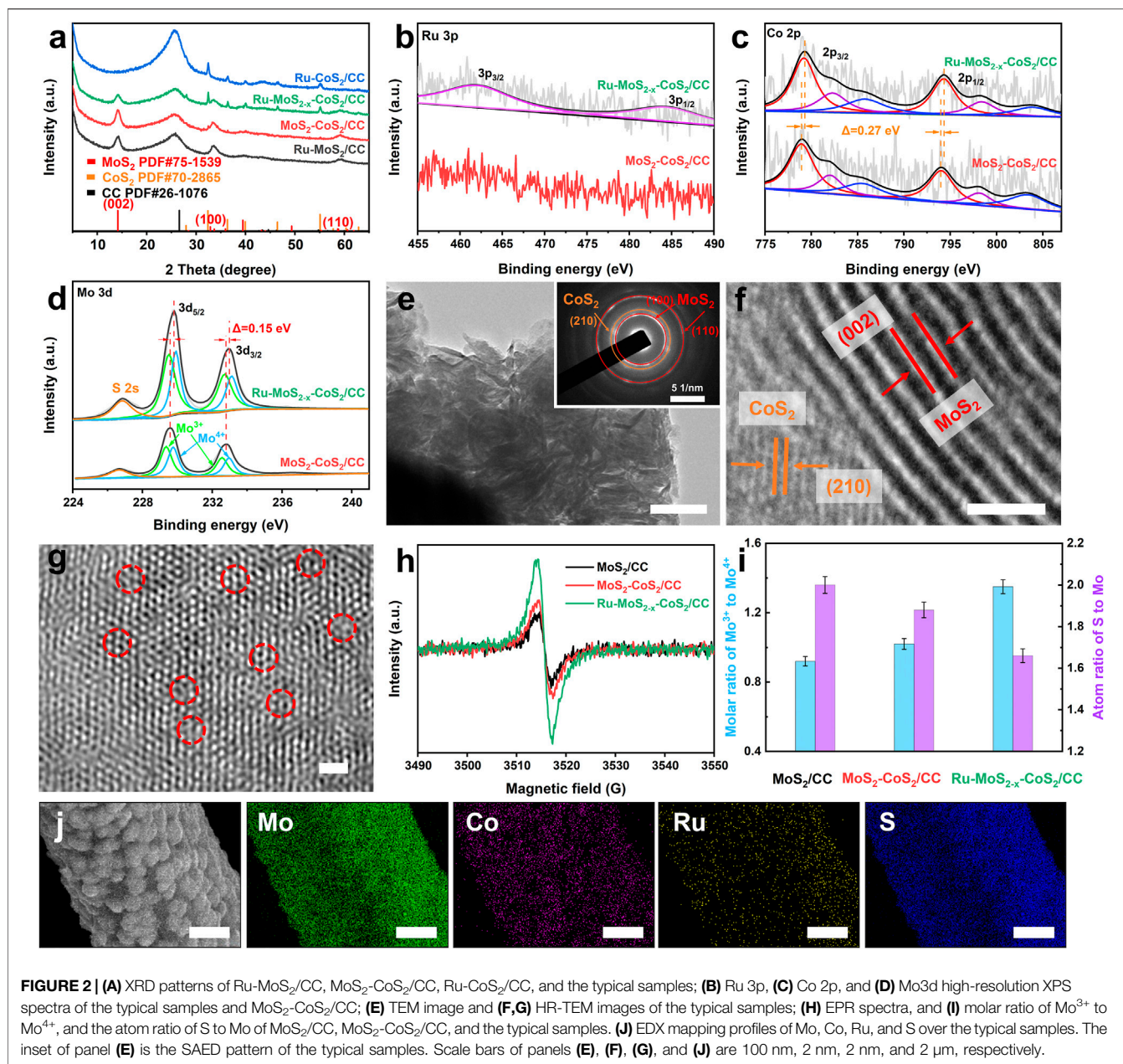
FIGURE 1 | Schematic representation of the fabrication of Ru-MoS₂-CoS₂/CC samples.

energy of hydrogen atoms (ΔG_H) of active sites to favor HER (Wang et al., 2015; Wang D. et al., 2019; Wang et al., 2021b). Among these TMs, ruthenium (Ru) belongs to the Pt group, but its price is as low as about 5% of Pt (Zhang J. et al., 2019). A quintessential example demonstrates that ΔG_H at the Ru-doped in-plane sulfur sites decreases to approximately 0.19 eV (Zhang X. et al., 2019). This indicates that doping Ru can efficiently modulate the electronic features of the adjacent sulfur atoms, thereby leading to the optimal H atom binding energy (Yan et al., 2018). On the other hand, after doping Ru into 2H-MoS₂ (Li J. et al., 2021) or 2H-WS₂ (Li J. et al., 2022), these Ru sites can significantly accelerate the water dissociation in alkaline environments. For example, the energy barrier of the H−OH cleavage (E) is as high as 2.42 eV before doping Ru. Remarkably, E of such Ru sites decreases to 2.02 eV, which is advantageous for water dissociation to OH and H intermediates.

Modulating S-vacancy into MoS₂-based materials has been developed as an efficient strategy (Tsai et al., 2017; Park et al., 2018; Li Y. et al., 2021) to activate inert basal planes because the exposed Mo atoms can be tailored into newborn active sites (Wang X. et al., 2020). Following this opinion, much effort has so far been devoted to introducing S-vacancy into the basal planes of mono-layered or multi-layered 2H-MoS₂ nanosheets (Li et al., 2016b; Tsai et al., 2017; Park et al., 2018; Li et al., 2019; Wang X. et al., 2020). Among these strategies, chemical vapor deposition coupled to plasma has been developed to modulate S-vacancy into MoS₂ (Li et al., 2016b). In this case, S atoms escape from the MoS₂ lattice more easily than Mo atoms due to the lower formation energy of S-vacancy compared to that of the Mo interstitial (Li et al., 2016b). Subsequently, the controllable electrochemical preparation of S-vacancy for multi-layered MoS₂ has been proposed by simply adjusting desulfurization parameters, such as desulfurization potential and time (Tsai et al., 2017). More recently, the single Ru atom doping technology promotes the phase transition of 2H-MoS₂ and the formation of S-vacancy, which greatly enhances its HER activity (Zhang J. et al., 2019). Nevertheless, a low or excessively high concentration of S-vacancy ($C_{S\text{-vacancy}}$) is disadvantageous for the hydrogen evolution reaction (HER)

activity of MoS₂-based materials. Consequently, it is of great importance for the development of a novel approach to fine-tuning $C_{S\text{-vacancy}}$ to significantly improve alkaline hydrogen evolution. In addition, the aforementioned electrocatalysts based on S-vacancy only consist of a single component (that is, MoS₂) rather than hybrid catalysts. As one of the traditional semiconductor materials, MoS₂ suffers from another drawback of unsatisfactory charge-transfer resistance (R_{CT}), leading to low HER activity (Li Y. et al., 2021; Wang et al., 2021b; Wang et al., 2021c). Hence, compositing with the metallic phase will favor fast electrode kinetics, realizing synergistically regulating $C_{S\text{-vacancy}}$ and R_{CT} of MoS₂-based electrocatalysts for highly efficient HER.

Herein, we develop a one-step Ru doping coupled to compositing with the CoS₂ strategy to synergistically regulate $C_{S\text{-vacancy}}$ of MoS₂-based materials for highly efficient alkaline HER. Ru doping is advantageous for the formation of S-vacancy in the basal planes of MoS₂. On the other hand, Ru doping favors heterogeneous nucleation and growth of CoS₂, which leads to rich heterogeneous interfaces between Ru-doped CoS₂ (Ru-CoS₂) and Ru-doped MoS₂₋ₓ (Ru-MoS₂₋ₓ). This facilitates the electron transfer from Ru-CoS₂ to Ru-MoS₂₋ₓ, thereby increasing $C_{S\text{-vacancy}}$ of MoS₂-based materials. At fixed Ru dopant, the electron injection effect increases gradually with an increase in the mass of Co precursor, which means more S²⁻ escaping from Ru-MoS₂ nanosheets. Therefore, synergistically regulating $C_{S\text{-vacancy}}$ of the as-synthesized samples, from 2.1 to 27.5%, is realized by a new one-step Ru doping coupled to compositing with the CoS₂ strategy. On regulating $C_{S\text{-vacancy}}$ to 17.1%, a balance between the intrinsic activity and the number of exposed Mo atoms (EMAs) to boost highly active EMAs should be realized. As a consequence, the typical samples demonstrate the optimal alkaline HER activity among all samples, such as a low overpotential of 170 mV at 100 mA cm⁻², a large specific alkaline HER current density of 77.6 μA cm⁻², and a turnover frequency of 4.29 s⁻¹ at -0.2 V as well as excellent long-term stability. Our results pave a novel approach to unlocking the potential of inert basal planes in MoS₂-based materials for highly efficient HER and promise important applications in the field of electrocatalytic hydrogen evolution.

FIGURE 2 | (A) XRD patterns of Ru-MoS₂/CC, MoS₂-CoS₂/CC, Ru-CoS₂/CC, and the typical samples; **(B)** Ru 3p, **(C)** Co 2p, and **(D)** Mo3d high-resolution XPS spectra of the typical samples and MoS₂-CoS₂/CC; **(E)** TEM image and **(F,G)** HR-TEM images of the typical samples; **(H)** EPR spectra, and **(I)** molar ratio of Mo^{3+} to Mo^{4+}, and the atom ratio of S to Mo of MoS₂/CC, MoS₂-CoS₂/CC, and the typical samples. **(J)** EDX mapping profiles of Mo, Co, Ru, and S over the typical samples. The inset of panel **(E)** is the SAED pattern of the typical samples. Scale bars of panels **(E)**, **(F)**, **(G)**, and **(J)** are 100 nm, 2 nm, 2 nm, and 2 μm, respectively.
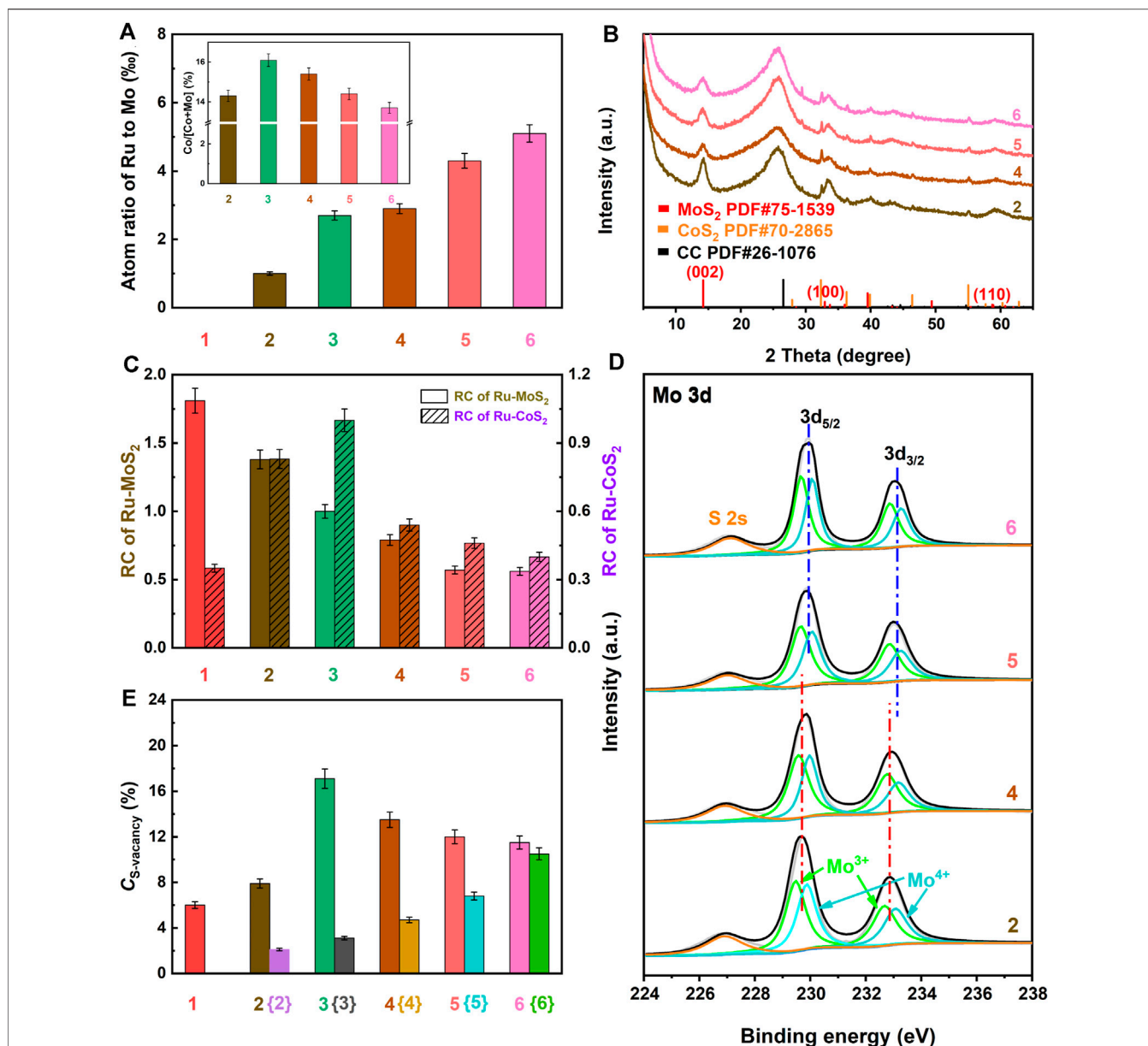
EXPERIMENTAL SECTION

Fabrication of the Typical Samples (Ru-MoS₂₋ₓ-CoS₂/CC)

The typical samples were synthesized by a one-pot hydrothermal strategy using the following precursors such as $Na_2MoO_4 \cdot 2H_2O$, CH_4N_2S, and $Co(NO_3)_2 \cdot 6H_2O$. In the typical experiments, 160 mg $Co(NO_3)_2 \cdot 6H_2O$, 160 mg $Na_2MoO_4 \cdot 2H_2O$, and 600 mg CH_4N_2S were dissolved in 46.0 ml deionized water under magnetic stirring. Subsequently, 4.0 ml $RuCl_3$ solution ($5 \, mmol \, L^{-1}$) was introduced into the above cobalt salt solution under magnetic stirring for 0.5 h. Carbon cloth (CC, 4 cm²) was pretreated

according to the related literature (Yu et al., 2015). Then, the above solution and the pretreated CC were transferred into a 100.0 ml Teflon-lined stainless-steel autoclave and heated to 200°C for 20 h. After the hydrothermal reaction, the mixture was cooled to room temperature. The typical samples were harvested after being washed with water thoroughly and vacuum-dried at 60 °C for 12.0 h and abbreviated as Ru-MoS₂₋ₓ-CoS₂/CC.

Fabrications of Other Ru-MoS₂₋ₓ-CoS₂/CC Samples

Other Ru-MoS₂₋ₓ-CoS₂/CC samples were synthesized at various volumes of $RuCl_3$ solution ($5 \, mmol \, L^{-1}$) of 1.0, 7.0, 10.0, and

FIGURE 3 | (A) Atom ratio of Ru to Mo based on ICP-OES, **(B)** XRD patterns, **(C)** RC of $Ru-MoS_{2-x}$ and $Ru-CoS_2$, **(D)** Mo3d high-resolution XPS spectra, and **(E)** $C_{S-vacancy}$ of the related samples. Meanwhile, 1, 2, 3, 4, 5 and 6 are denoted as MoS_2-CoS_2/CC, $Ru-MoS_{2-x}-CoS_2/CC-1.0$, the typical samples, $Ru-MoS_{2-x}-CoS_2/CC-7.0$, $Ru-MoS_{2-x}-CoS_2/CC-10.0$, and $Ru-MoS_{2-x}-CoS_2/CC-30.0$, respectively. Fabrications of {2}, {3}, {4}, {5}, and {6} are the same as those of $Ru-MoS_{2-x}-CoS_2/CC-1.0$, the typical samples, $Ru-MoS_{2-x}-CoS_2/CC-7.0$, $Ru-MoS_{2-x}-CoS_2/CC-10.0$, and $Ru-MoS_{2-x}-CoS_2/CC-30.0$ except for the absence of $Co(NO_3)_2$, to be denoted as $Ru-MoS_2/CC-1.0$, $Ru-MoS_2/CC$, $Ru-MoS_2/CC-7.0$, $Ru-MoS_2/CC-10.0$, and $Ru-MoS_2/CC-30.0$, respectively. The inset of panel **(A)** is the atom ratio of Co to (Co + Mo) of the related samples based on ICP-OES.

30.0 ml under otherwise similar conditions as the typical experiments. These $Ru-MoS_{2-x}-CoS_2/CC$ samples are denoted as $Ru-MoS_{2-x}-CoS_2/CC-1.0$, $Ru-MoS_{2-x}-CoS_2/CC-7.0$, $Ru-MoS_{2-x}-CoS_2/CC-10.0$, and $Ru-MoS_{2-x}-CoS_2/CC-30.0$.

In addition, $Ru-MoS_{2-x}-CoS_2/CC-80$, $Ru-MoS_{2-x}-CoS_2/CC-240$, $Ru-MoS_{2-x}-CoS_2/CC-280$, and $Ru-MoS_{2-x}-CoS_2/CC-320$ were synthesized at various masses of $Co(NO_3)_2·6H_2O$ of 80, 240, 280, and 320 mg under otherwise similar conditions of the typical experiments, respectively.

Figure 1 displays a schematic representation of the fabrication of all $Ru-MoS_{2-x}-CoS_2/CC$ samples.

Fabrications of Ru-MoS₂/CC, MoS₂/CC, MoS₂-CoS₂/CC, and Ru-CoS₂/CC

Ru-doped MoS_2 nanosheets assembled on CC are abbreviated as $Ru-MoS_2/CC$. Fabrication of $Ru-MoS_2/CC$ is almost the same as the typical samples except for the absence of $Co(NO_3)_2$.

MoS_2 nanosheets assembled on CC are abbreviated as MoS_2/CC. Fabrication of MoS_2/CC is almost the same as Ru-MoS_2/CC except for the absence of $RuCl_3$ solution.

MoS_2 nanosheets coated with CoS_2 assembled on CC are abbreviated as MoS_2-CoS_2/CC. Fabrication of MoS_2-CoS_2/CC is almost the same as the typical samples except for the absence of $RuCl_3$ solution.

Ru-doped CoS_2 assembled on CC are abbreviated as Ru-CoS_2/CC. Fabrication of Ru-CoS_2/CC is almost similar to the typical samples except for the absence of $Na_2MoO_4.2H_2O$.

Other experimental details about materials, characterization, and performance measurements are supplied in **Supplementary Material S1**.

RESULTS AND DISCUSSION

Characterization of the Typical Samples

Scanning electron microscopic (SEM) images display the morphology of the typical samples in **Supplementary Figures SJ–L**. From these figures, it can be observed that lots of nanosheets are grown on the smooth surface of CC (**Supplementary Figure S2**). Powder X-ray diffraction (XRD) pattern of Ru-MoS_{2-x}-CoS_2/CC (**Figure 2A**) shows the diffraction peaks located at $2\theta = 14.1°$, $32.7°$, and $58.8°$, matching well with the (002), (100), and (110) planes of 2H-MoS_2 (PDF#75-1539) (Nguyen et al., 2021), respectively. Other sharp diffraction peaks of Ru-MoS_{2-x}-CoS_2/CC, such as $32.4°$ and $55.1°$, are attributed to the (200) and 311) planes of CoS_2 (PDF#70-2865) (Yao et al., 2019), respectively, suggesting the presence of highly crystallized CoS_2 besides 2H-MoS_2. From **Figure 2A**, we also observe the diffraction peak at $26.2°$ originating from CC. The Raman spectrum of Ru-MoS_{2-x}-CoS_2/CC (**Supplementary Figure S3**) displays the typical E_{2g}^1 and A_{1g} vibration models of the Mo-S bonds, further verifying the phase structure of 2H-MoS_2 in Ru-MoS_{2-x}-CoS_2/CC. As shown in **Figure 2B**, the Ru 3p high-resolution X-ray photoelectron spectroscopy (XPS) spectrum of Ru-MoS_{2-x}-CoS_2/CC is divided into two characteristic peaks at the binding energies of 462.4 and 484.7 eV, corresponding to Ru $3p_{3/2}$ and Ru $3p_{1/2}$ (Ge et al., 2022). Nevertheless, no peak of Ru is detected in MoS_2 nanosheets coated with CoS_2 assembled on CC (MoS_2-CoS_2/CC) in **Figure 2B**. Furthermore, **Figures 2C, D** exhibit Co 2p and Mo 3 day XPS spectra of Ru-MoS_{2-x}-CoS_2/CC, respectively. It is seen that Co 2p and Mo 3 day peaks positively shift by about 0.27 and 0.15 eV compared to those of MoS_2-CoS_2/CC (Hao et al., 2017), respectively. Additionally, the characteristic peaks about Ru_2S_3 or $RuCl_3$ are not observed in the XRD pattern of Ru-MoS_{2-x}-CoS_2/CC (**Figure 2A**). Therefore, these data confirm the successful doping of Ru into the following two phases of Ru-MoS_{2-x}-CoS_2/CC, 2H-MoS_2, and CoS_2.

Nanosheets of Ru-MoS_{2-x}-CoS_2/CC are also clearly observed from transmission electron microscopic (TEM) image (**Figure 2E**), which is consistent with the results of SEM images. According to the high-resolution TEM (HR-TEM) image (**Figure 2F**), the lattice spacings of 0.625 and 0.245 nm that are seen in Ru-MoS_{2-x}-CoS_2/CC correspond to the (002) plane of MoS_2 and the (210) plane of CoS_2 (He et al., 2020; Liu X.

et al., 2022), respectively. These also conform to the results of XRD. As we know, MoS_2 is regarded as one of the traditional semiconductor materials, and CoS_2 is a metallic phase due to its high Fermi level. Therefore, there are lots of Schottky heterojunctions among Ru-MoS_{2-x}-CoS_2/CC. In addition, the inset of **Figure 2E** (selected area electron diffraction, SAED) pattern indicates that Ru-doped MoS_2 (Ru-MoS_2) and Ru-doped CoS_2 (Ru-CoS_2) of Ru-MoS_{2-x}-CoS_2/CC are polycrystalline (Huang et al., 2015). We can clearly observe that many defects exist in such Ru-MoS_2 from **Figure 2G** due to lattice distortion by Ru doping (Zhang J. et al., 2019) and the electron injection effect (Gan et al., 2018; Zhang J. et al., 2019). Energy-dispersive X-ray (EDX) spectroscopy mapping (**Figure 2J**) profiles further confirm the uniform distribution of Mo, Co, Ru, and S elements throughout Ru-MoS_{2-x}-CoS_2/CC. Considering that Ru-MoS_2 assembled on CC (Ru-MoS_2/CC) and Ru-CoS_2 assembled on CC (Ru-CoS_2/CC) tend to form nanosheets (**Supplementary Figures S1B, C**) and nanoparticles (**Supplementary Figures SH, I**), respectively, and that Ru-CoS_2 nucleates and grows prior to Ru-MoS_2 (**Figures 4A–F**), we can reasonably deduce as follows: during the hydrothermal process, Ru-CoS_2 nanoparticles are firstly assembled on CC; then, Ru-CoS_2/CC are densely coated by Ru-MoS_2 nanosheets to construct the typical samples, Ru-MoS_{2-x}-CoS_2/CC.

According to XPS data in **Figure 2D** and **Supplementary Figure S4**, we characterize molar ratios of Mo^{3+} to Mo^{4+} of MoS_2/CC, MoS_2-CoS_2/CC, and Ru-MoS_{2-x}-CoS_2/CC in **Figure 2I**. The presence of Mo^{3+} can induce S-vacancy of the basal planes in Ru-MoS_2 (Ma et al., 2020) of Ru-MoS_{2-x}-CoS_2/CC. From **Figure 2I**, Ru-MoS_{2-x}-CoS_2/CC exhibits a higher value of about the molar ratio of Mo^{3+} to Mo^{4+} than MoS_2/CC or MoS_2-CoS_2/CC, reaching 1.35. To confirm such defective structures, electron paramagnetic resonance (EPR) (Liu et al., 2017; Gong et al., 2020; Wang J. et al., 2021) is further employed to estimate the S-vacancy of all samples. As expected, Ru-MoS_{2-x}-CoS_2/CC demonstrates the highest EPR signal at g = ~ 2.002 among all samples (**Figure 2H**). Moreover, the EPR signal of MoS_2-CoS_2/CC is higher than that of MoS_2/CC. These data straightforwardly indicate that the formation of S-vacancy might be closely related to both Ru doping into MoS_2 and compositing with CoS_2.

Doping Ru Coupled to Compositing With CoS_2 to Regulate Microstructures of the As-synthesized Samples

First, a series of Ru-MoS_2/CC samples were synthesized at the various volumes of $RuCl_3$ solution (V) of 1.0, 4.0, 7.0, 10.0, and 30.0 ml under otherwise similar conditions of the typical experiments except for the absence of $Co(NO_3)_2$. These Ru-MoS_2/CC samples are denoted as Ru-MoS_2/CC-1.0, Ru-MoS_2/CC-7.0, Ru-MoS_2/CC-10.0, and Ru-MoS_2/CC-30.0. Similar Ru 3p XPS spectra to the typical samples are observed in **Supplementary Figure S5A**, which is responsible for successfully doping Ru into all Ru-MoS_2/CC samples. In addition, the atom ratios of Ru to Mo (A) of all Ru-MoS_2/CC samples are characterized by XPS in **Supplementary Figure S5B**. From this figure, A increases with increasing V, indicating that

more Ru will be doped into the Ru-MoS$_2$/CC samples at higher V. In this work, the atomic ratio of S to Mo (S: Mo) of MoS$_2$/CC is firstly measured (**Supplementary Table S1**) and is normalized to 2.00. Then, it is employed as a reference to confirm the normalized S: Mo of MoS$_{2-x}$ in all Ru-MoS$_2$/CC samples in terms of XPS data (Xu et al., 2016; Wang J. et al., 2021). Here, the measured S: Mo for all Ru-MoS$_2$/CC samples are the atom ratios of S minus double Ru to Mo, which is abbreviated as [(S–2Ru)/Mo]. Therefore, the normalized S: Mo of MoS$_{2-x}$ in all samples are listed in **Supplementary Table S2**. From **Figure 3E**, $C_{\text{S-vacancy}}$ of Ru-MoS$_2$/CC samples increases with the increase in Ru dopants. For example, $C_{\text{S-vacancy}}$ of Ru-MoS$_2$/CC-30.0 increases to 10.5% at $V = 30.0$ ml. That is to say, doping Ru can regulate $C_{\text{S-vacancy}}$ of Ru-MoS$_2$/CC samples varying from 2.1 to 10.5%.

Density functional theory (DFT) calculation reveals that the Ru-S bonding energy (about 0.92 eV) decreases by 0.87 eV compared to the Mo-S bonding energy (about 1.79 eV) (Luo et al., 2020), which is advantageous for the formation of S-vacancy in the basal planes of MoS$_2$. In this work, Ru atoms substituting for Mo atoms in MoS$_2$ are abbreviated as Ru$_{(Mo)}$. According to the previously reported literature (Zhang J. et al., 2019; Zhang X. et al., 2019), Ru doping results in an increase in $C_{\text{S-vacancy}}$ due to the strong attractive interaction between Ru$_{(Mo)}$ and the adjacent S-vacancy. Furthermore, S-vacancy is exclusively stable around Ru$_{(Mo)}$ (Kang, 2021).

To investigate the synergistic effect of doping Ru coupled to compositing with CoS$_2$ on the microstructure, other Ru-MoS$_{2-x}$-CoS$_2$/CC samples are further synthesized at various V of 1.0, 7.0, 10.0, and 30.0 ml under otherwise similar conditions of the typical experiments to be denoted as Ru-MoS$_{2-x}$-CoS$_2$/CC-1.0, Ru-MoS$_{2-x}$-CoS$_2$/CC-7.0, Ru-MoS$_{2-x}$-CoS$_2$/CC-10.0, and Ru-MoS$_{2-x}$-CoS$_2$/CC-30.0, respectively. According to **Supplementary Figure S6**, these Ru-MoS$_{2-x}$-CoS$_2$/CC samples almost display the same Ru 3p XPS spectra as the typical samples, indicating a successful doping of Ru into them as well. The values of A of all samples are characterized by inductively coupled plasma-optical emission spectroscopy (ICP-OES). In terms of **Figure 3A**, the values of A of these samples increase with the increase in V. Moreover, other Ru-MoS$_{2-x}$-CoS$_2$/CC samples also exhibit the same phase structure as the typical samples, since the XRD pattern of each sample is similar to that of the typical samples (**Figure 3B**). **Figure 3C** further presents the relative crystallinity (RC) of Ru-MoS$_{2-x}$ and Ru-CoS$_2$ for all Ru-MoS$_{2-x}$-CoS$_2$/CC samples based on the corresponding XRD data such as the (002) plane for molybdenum disulfide and (200) (210) (211) (220), and 311) planes for cobalt disulfide. From this figure, the RC of Ru-MoS$_{2-x}$ decreases with the increase in V, which implies that more defective structures or S-vacancy would be modulated into the basal planes of Ru-MoS$_{2-x}$ at higher V. However, the influence of V on RC of Ru-CoS$_2$ is not coincident with the trend of the former. Initially, the RC of Ru-CoS$_2$ gradually increases with increasing V. At $V = 4.0$ ml, the RC of Ru-CoS$_2$ of the typical samples exhibits the highest value among all samples. However, further increasing V leads to a decrease in the RC of Ru-CoS$_2$.

In addition, Mo^{3+} can be observed in Mo 3 day XPS spectra of all Ru-MoS$_{2-x}$-CoS$_2$/CC samples (**Figure 3D**), implying the formation of S-vacancy of the basal planes in Ru-MoS$_{2-x}$. Taking into account that MoS$_2$-CoS$_2$/CC and other Ru-MoS$_{2-x}$-CoS$_2$/CC samples (**Supplementary Figures S1E, F**; **Supplementary Figure S7**) are almost similar to the morphology of the typical samples (**Supplementary Figures S1K, L**), such core–shell structure, Ru-MoS$_{2-x}$ nanosheets densely coated Ru-CoS$_2$ composites, facilitates to correctly reflect the S: Mo of Ru-MoS$_{2-x}$ in all samples by XPS analysis. As mentioned above, the S: Mo of MoS$_2$/CC is also employed as a reference to confirm the normalized S: Mo of Ru-MoS$_{2-x}$ in all Ru-MoS$_{2-x}$-CoS$_2$/CC samples (Li et al., 2016a; Xu et al., 2016) based on XPS data (**Supplementary Figure S8**). Here, the measured S: Mo for all Ru-MoS$_{2-x}$-CoS$_2$/CC samples is the atom ratio of S minus double (Co + Ru) to Mo, which is abbreviated as [(S–2Co–2Ru)/Mo]. Subsequently, we further calculate the related $C_{\text{S-vacancy}}$, as shown in **Figure 3E**; **Supplementary Table S1**. From **Figure 3E**, $C_{\text{S-vacancy}}$ of Ru-MoS$_{2-x}$-CoS$_2$/CC increases to 7.9% compared to that of MoS$_2$-CoS$_2$/CC (about 6.0%). Out of expectation, $C_{\text{S-vacancy}}$ of the typical samples rather than Ru-MoS$_{2-x}$-CoS$_2$/CC-30.0 reaches the highest value among all samples, about 17.1% from **Figure 3E**. At the same time, Ru-MoS$_{2-x}$-CoS$_2$/CC-30.0 exhibits a lower EPR signal than the typical samples (**Supplementary Figure S9**), further confirming fewer S-vacancy for Ru-MoS$_{2-x}$-CoS$_2$/CC-30.0 in comparison with the typical samples. In other words, at a fixed mass of Co precursor, $C_{\text{S-vacancy}}$ of Ru-MoS$_{2-x}$ can be precisely regulated from 7.9 to 17.1% by synergistic Ru doping and compositing with CoS$_2$ engineering. As a consequence, we can infer that compositing with CoS$_2$ should be another key factor to regulate $C_{\text{S-vacancy}}$ of Ru-MoS$_{2-x}$ nanosheets in Ru-MoS$_{2-x}$-CoS$_2$/CC samples. This is because Ru doping also affects the microstructure of CoS$_2$, which may have a significant influence on $C_{\text{S-vacancy}}$ of Ru-MoS$_{2-x}$ nanosheets in Ru-MoS$_{2-x}$-CoS$_2$/CC samples in turn.

Following this viewpoint, we deeply investigate the influence of doping Ru on the microstructure of cobalt disulfide. As mentioned above, CoS$_2$ nucleates and grows prior to MoS$_2$. To eliminate the effect of MoS$_2$ as much as possible during the characterization of microstructures of CoS$_2$, the related samples such as [MoS$_2$-CoS$_2$/CC], [1] [Ru-MoS$_{2-x}$-CoS$_2$/CC], [2], [3], and [4] are synthesized at $t = 6$ h (**Figures 4A–F**) rather than 20 h. Fabrications of [MoS$_2$-CoS$_2$/CC], [1] [Ru-MoS$_{2-x}$-CoS$_2$/CC], [2], [3], and [4] are the same as those of MoS$_2$-CoS$_2$/CC, Ru-MoS$_{2-x}$-CoS$_2$/CC-1.0, the typical samples, Ru-MoS$_{2-x}$-CoS$_2$/CC-7.0, Ru-MoS$_{2-x}$-CoS$_2$/CC-10.0, and Ru-MoS$_{2-x}$-CoS$_2$/CC-30.0 except for t, respectively. Their SEM images and XRD patterns are displayed in **Figures 4A–G**, respectively. Besides the diffraction peak at 26.2° of CC, other peaks are indexed to CoS$_2$ without the signal of MoS$_2$ for all samples (**Figure 4G**), further confirming the heterogeneous nucleation and growth of CoS$_2$ prior to MoS$_2$. As shown in **Figure 4A**, a small number of spherical CoS$_2$ nanoparticles are grown on CC for [MoS$_2$-CoS$_2$/CC]. Moreover, the similar phenomena are observed for Ru-doped samples from **Figures 4B–F**. Interestingly, with an increase in V, the size and number of Ru-CoS$_2$ nanoparticles gradually increase (**Figure 4B**). At $V = 4.0$ ml, both the size and number of Ru-CoS$_2$ nanoparticles for [Ru-MoS$_{2-x}$-CoS$_2$/CC] reach up to the maximum value (**Figure 4C**). However, further increasing V leads to a decrease in both the size and number of Ru-CoS$_2$
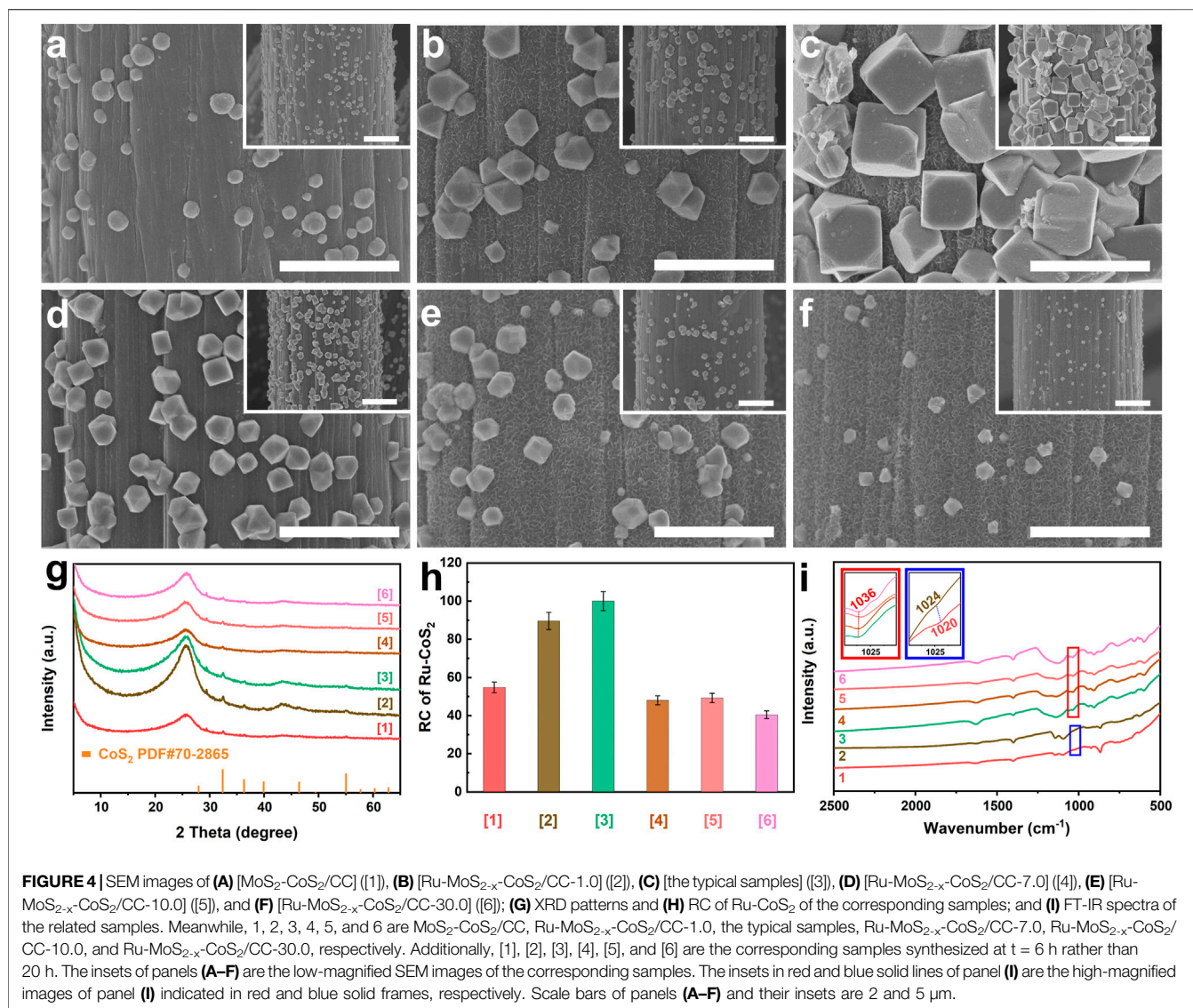
FIGURE 4 | SEM images of **(A)** [MoS$_2$-CoS$_2$/CC] ([1]), **(B)** [Ru-MoS$_{2-x}$-CoS$_2$/CC-1.0] ([2]), **(C)** [the typical samples] ([3]), **(D)** [Ru-MoS$_{2-x}$-CoS$_2$/CC-7.0] ([4]), **(E)** [Ru-MoS$_{2-x}$-CoS$_2$/CC-10.0] ([5]), and **(F)** [Ru-MoS$_{2-x}$-CoS$_2$/CC-30.0] ([6]); **(G)** XRD patterns and **(H)** RC of Ru-CoS$_2$ of the corresponding samples; and **(I)** FT-IR spectra of the related samples. Meanwhile, 1, 2, 3, 4, 5, and 6 are MoS$_2$-CoS$_2$/CC, Ru-MoS$_{2-x}$-CoS$_2$/CC-1.0, the typical samples, Ru-MoS$_{2-x}$-CoS$_2$/CC-7.0, Ru-MoS$_{2-x}$-CoS$_2$/CC-10.0, and Ru-MoS$_{2-x}$-CoS$_2$/CC-30.0, respectively. Additionally, [1], [2], [3], [4], [5], and [6] are the corresponding samples synthesized at t = 6 h rather than 20 h. The insets of panels **(A–F)** are the low-magnified SEM images of the corresponding samples. The insets in red and blue solid lines of panel **(I)** are the high-magnified images of panel **(I)** indicated in red and blue solid frames, respectively. Scale bars of panels **(A–F)** and their insets are 2 and 5 μm.

for other [Ru-MoS$_{2-x}$-CoS$_2$/CC] (**Figures 4D–F**). Next, we characterize the RC of Ru-CoS$_2$ for all samples synthesized at 6 h according to XRD data such as (200) (210), (211) (220), and (311) planes of cobalt disulfide, as shown in **Figure 4H**. Impressively, their trend in the variation is almost consistent with that of the RC of Ru-CoS$_2$ of Ru-MoS$_{2-x}$-CoS$_2$/CC samples synthesized at 20 h (**Figure 3C**). This confirms that doping Ru can improve the crystallinity of CoS$_2$ under certain conditions. To find out the reason for this issue, we investigate the Fourier-transforming infrared (FT-IR) spectrum of MoS$_2$-CoS$_2$/CC in **Figure 4I**. The peak located at 1020 cm^{-1} straightforwardly indicates the formation of CoS$_2$ (Chakraborty et al., 2006) at V = 0.0 ml. At V increasing to 1.0 ml, the peak of Ru-MoS$_{2-x}$-CoS$_2$/CC-1.0 located at 1024 cm^{-1} shows a blue-shift of about 4 cm^{-1} compared to that of MoS$_2$-CoS$_2$/CC. At V = 4.0 ml, the related peak blue-shifts to about 1036 cm^{-1}, as shown in **Figure 4I**. This indicates that doping Ru into CoS$_2$ can decrease the Co–S bond length and enhance the bonding

energy (Feng et al., 2018), which favors the formation of Ru-CoS$_2$. However, a decrease in both the size and number of CoS$_2$ with further increasing V (**Figures 4D–F**) can be explained as follows: introducing excessive Ru into the lattice of CoS$_2$ may induce an increase in the oxidation state of neighboring Co ions to maintain the charge neutrality. The similar result has been observed for other transition metal compounds, such as NiO (Smyth, 2000; Ge et al., 2022). This implies that excessive dopant will hinder the formation of CoS$_2$ in turn.

Possible Formation Mechanism of S-Vacancy in Ru-MoS$_{2-x}$-CoS$_2$/CC Samples

Based on these results and discussion, a possible formation mechanism of S-vacancy of the basal planes in Ru-MoS$_{2-x}$ of Ru-MoS$_{2-x}$-CoS$_2$/CC samples can be proposed as follows: on the one side, S-vacancy is modulated into the basal planes of MoS$_2$ due to the strong attractive interaction between Ru$_{(Mo)}$ and the

FIGURE 5 | Schematic illustration of the possible formation mechanism of the S-vacancy of the basal planes in Ru-MoS$_{2-x}$ of Ru-MoS$_{2-x}$-CoS$_2$/CC samples.
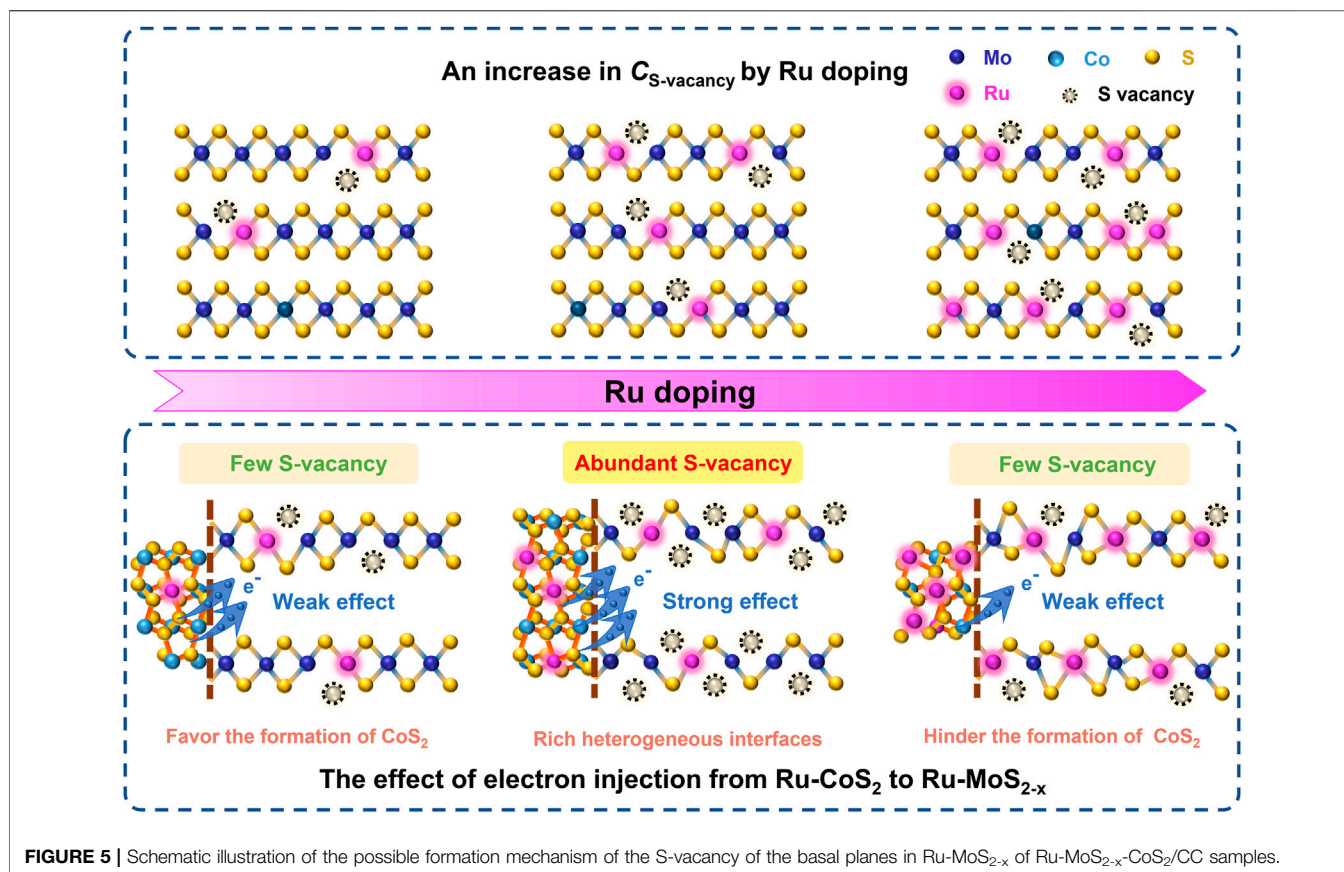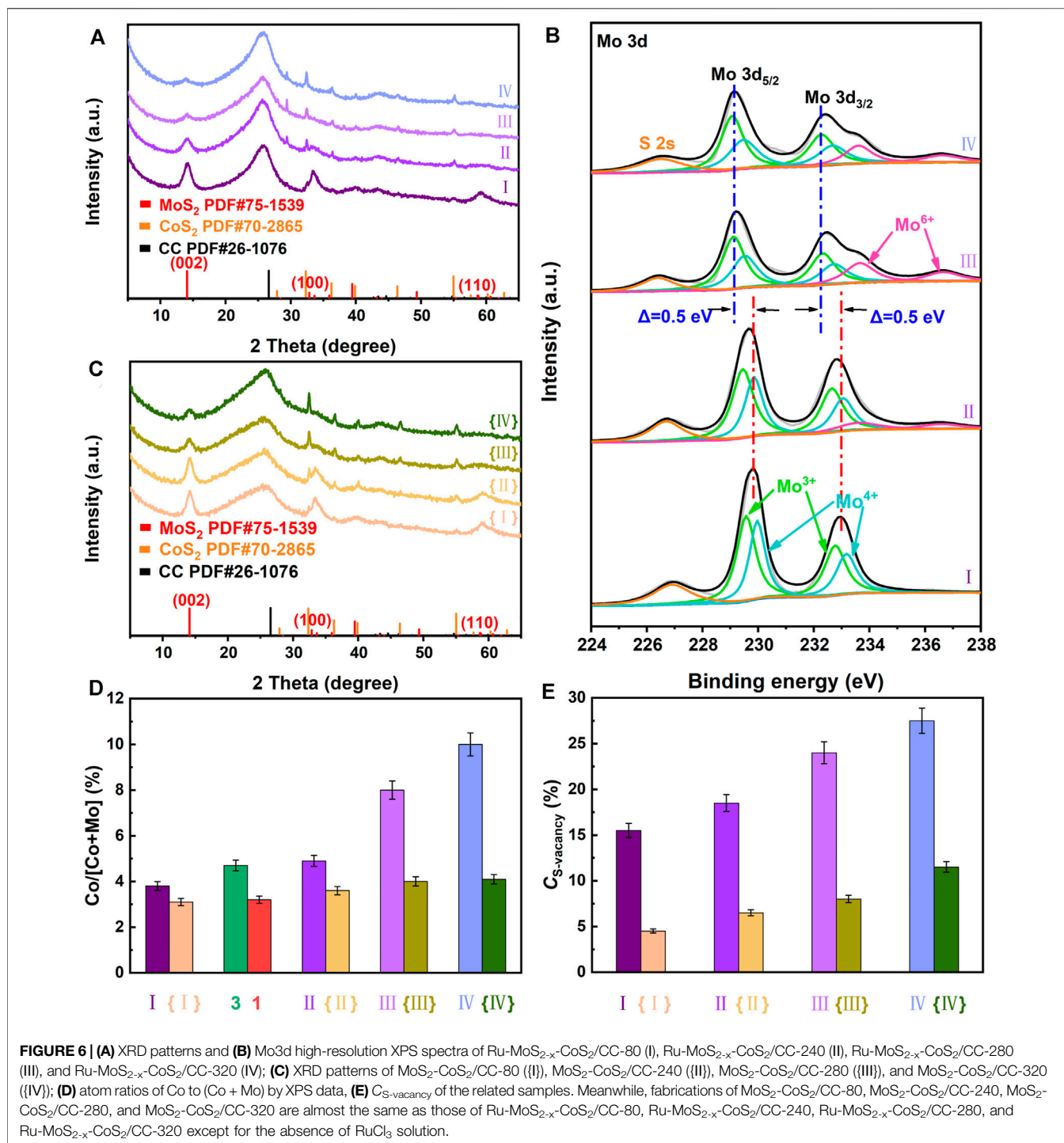
adjacent S-vacancy. Furthermore, S-vacancy is exclusively stable around Ru$_{(Mo)}$. On the other hand, by compositing with CoS$_2$, Schottky heterojunctions provide a feasible opportunity for the electron transfer from Ru-CoS$_2$ to Ru-MoS$_{2-x}$ (Li et al., 2018) due to a high Fermi level of CoS$_2$. This effect can promote S^{2-} escaping from Ru-MoS$_{2-x}$ nanosheets to remain charge neutrality (Liu et al., 2017; Gan et al., 2018), indicating the formation of the positively charged defects, S-vacancy. Subsequently, we further characterize the atom ratios of Co to (Co + Mo) of the related samples by ICP-OES in the inset of **Figure 3A**. From this inset, the atom ratio of Co to (Co + Mo) of the typical samples is as high as about 16.1% at V increasing to 4.0 ml, thereby resulting in more Ru-CoS$_2$, and rich heterogeneous interfaces between Ru-CoS$_2$ and Ru-MoS$_{2-x}$ as well. More heterogeneous interfaces favor the electron injection from Ru-CoS$_2$ to Ru-MoS$_{2-x}$, which leads to an increase in $C_{S-vacancy}$ (**Figure 3E**). However, further increasing V results in a decrease in atom ratios of Co to (Co + Mo) (inset of **Figure 3A**) and poor heterojunctions. This could indicate a weaker electron injection effect of Ru-CoS$_2$ and lower $C_{S-vacancy}$ at excessively high V. The schematic illustration of the possible formation mechanism of S-vacancy of the basal planes in Ru-MoS$_{2-x}$ of Ru-MoS$_{2-x}$-CoS$_2$/CC samples is presented in **Figure 5**.
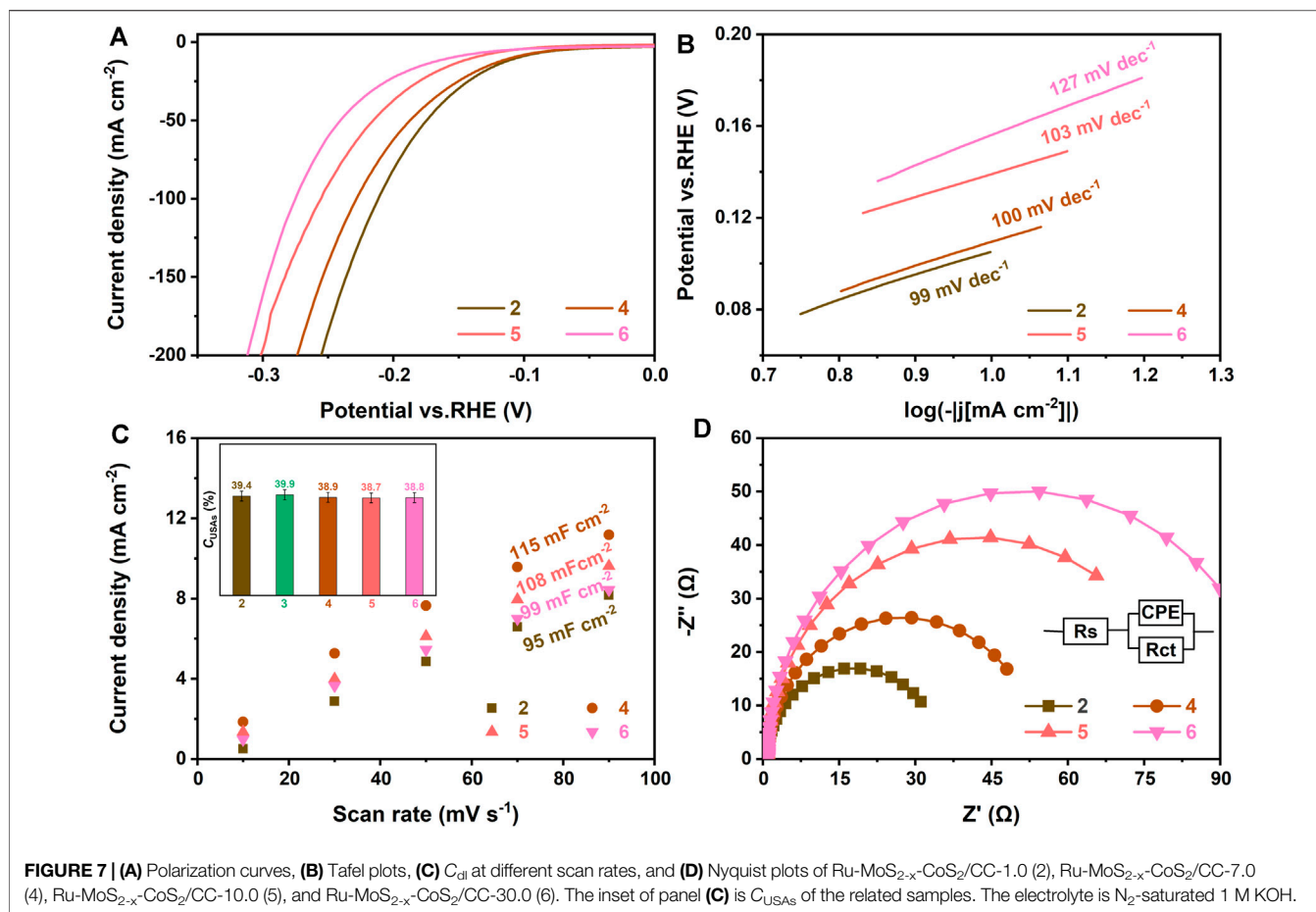
To confirm this viewpoint, we systematically investigate the effect of compositing with CoS$_2$ on $C_{S-vacancy}$ of the as-

synthesized samples at fixed V or Ru dopants in **Figure 6**. **Figure 6A** exhibits XRD patterns of Ru-MoS$_{2-x}$-CoS$_2$/CC-80, Ru-MoS$_{2-x}$-CoS$_2$/CC -240, Ru-MoS$_{2-x}$-CoS$_2$/CC-280, and Ru-MoS$_{2-x}$-CoS$_2$/CC-320. With an increase in the mass of Co precursor (m_{Co}), the intensity of the diffraction peak of the (002) plane at 14.1° for Ru-MoS$_{2-x}$ greatly decreases, while intensities of peaks of the (200) and 311) planes for Ru-CoS$_2$ gradually increase (**Figure 6A**), indicating a decrease in the RC of Ru-MoS$_{2-x}$ and an increase in the RC of Ru-CoS$_2$ (**Supplementary Figure S10**). At m_{Co} increasing to 240 mg, Ru-CoS$_2$ can be densely coated by Ru-MoS$_{2-x}$ nanosheets (**Supplementary Figure S11B**). Nevertheless, further increasing m_{Co} to 280 or 320 mg leads to incompact Ru-MoS$_{2-x}$ shells (**Supplementary Figures S11C, D**) due to the formation of more Ru-CoS$_2$ or a decrease in the content of Ru-MoS$_{2-x}$. These data are in good agreement with the results of **Figure 6D**, which displays atom ratios of Co to (Co + Mo) of the as-synthesized samples by XPS analysis. These atom ratios also increase with increasing m_{Co}. For example, the atom ratio of Co to (Co + Mo) of R Ru-MoS$_{2-x}$-CoS$_2$/CC-320 increases up to 10.1%. To further confirm the effect of electron injection from Ru-CoS$_2$ to Ru-MoS$_{2-x}$, we characterize Mo3d high-resolution XPS spectra of Ru-MoS$_{2-x}$-CoS$_2$/CC-80, Ru-MoS$_{2-x}$-CoS$_2$/CC-240, Ru-MoS$_{2-x}$-CoS$_2$/CC-280, and Ru-MoS$_{2-x}$-CoS$_2$/CC-320 in **Figure 6B**. Mo 3 days in XPS data move to low binding energy (Huang et al., 2019), implying an increase in the electron density

FIGURE 6 | (A) XRD patterns and **(B)** Mo3d high-resolution XPS spectra of Ru-MoS$_{2-x}$-CoS$_2$/CC-80 (I), Ru-MoS$_{2-x}$-CoS$_2$/CC-240 (II), Ru-MoS$_{2-x}$-CoS$_2$/CC-280 (III), and Ru-MoS$_{2-x}$-CoS$_2$/CC-320 (IV); **(C)** XRD patterns of MoS$_2$-CoS$_2$/CC-80 ({I}), MoS$_2$-CoS$_2$/CC-240 ({II}), MoS$_2$-CoS$_2$/CC-280 ({III}), and MoS$_2$-CoS$_2$/CC-320 ({IV}); **(D)** atom ratios of Co to (Co + Mo) by XPS data, **(E)** $C_{S\text{-vacancy}}$ of the related samples. Meanwhile, fabrications of MoS$_2$-CoS$_2$/CC-80, MoS$_2$-CoS$_2$/CC-240, MoS$_2$-CoS$_2$/CC-280, and MoS$_2$-CoS$_2$/CC-320 are almost the same as those of Ru-MoS$_{2-x}$-CoS$_2$/CC-80, Ru-MoS$_{2-x}$-CoS$_2$/CC-240, Ru-MoS$_{2-x}$-CoS$_2$/CC-280, and Ru-MoS$_{2-x}$-CoS$_2$/CC-320 except for the absence of RuCl$_3$ solution.

of Ru-MoS$_{2-x}$ of the as-synthesized samples. For example, Mo 3 day peaks of the typical samples negatively shift by about 0.06 eV compared to those of Ru-MoS$_{2-x}$-CoS$_2$/CC-80 in terms of **Figure 2D** and **Figure 6B**. After careful investigations, similar results are observed in Mo3d XPS spectra of other Ru-MoS$_{2-x}$-CoS$_2$/CC samples (**Figure 6B**), yielding the related data about negative shifts of 0.12 eV for Ru-MoS$_{2-x}$-CoS$_2$/CC-240, 0.45 eV for Ru-MoS$_{2-x}$-CoS$_2$/CC-280, and 0.50 eV for Ru-MoS$_{2-x}$-CoS$_2$/

CC-320. It is seen that such an electron injection effect increases gradually with the increase in m_{Co}, which means more S^{2-} escaping from MoS$_{2-x}$ nanosheets (Liu et al., 2017; Gan et al., 2018) at higher m_{Co}. Therefore, the atom ratios of S to Mo for all Ru-MoS$_{2-x}$-CoS$_2$/CC samples decrease (**Supplementary Table S3**), and $C_{S\text{-vacancy}}$ increases (**Figure 6E**) with increasing m_{Co}. For instance, Ru-MoS$_{2-x}$-CoS$_2$/CC-320 demonstrate the highest $C_{S\text{-vacancy}}$ (about 27.5%) among all samples.

FIGURE 7 | **(A)** Polarization curves, **(B)** Tafel plots, **(C)** C_{dl} at different scan rates, and **(D)** Nyquist plots of Ru-MoS$_{2-x}$-CoS$_2$/CC-1.0 (2), Ru-MoS$_{2-x}$-CoS$_2$/CC-7.0 (4), Ru-MoS$_{2-x}$-CoS$_2$/CC-10.0 (5), and Ru-MoS$_{2-x}$-CoS$_2$/CC-30.0 (6). The inset of panel **(C)** is C_{USAs} of the related samples. The electrolyte is N$_2$-saturated 1 M KOH.
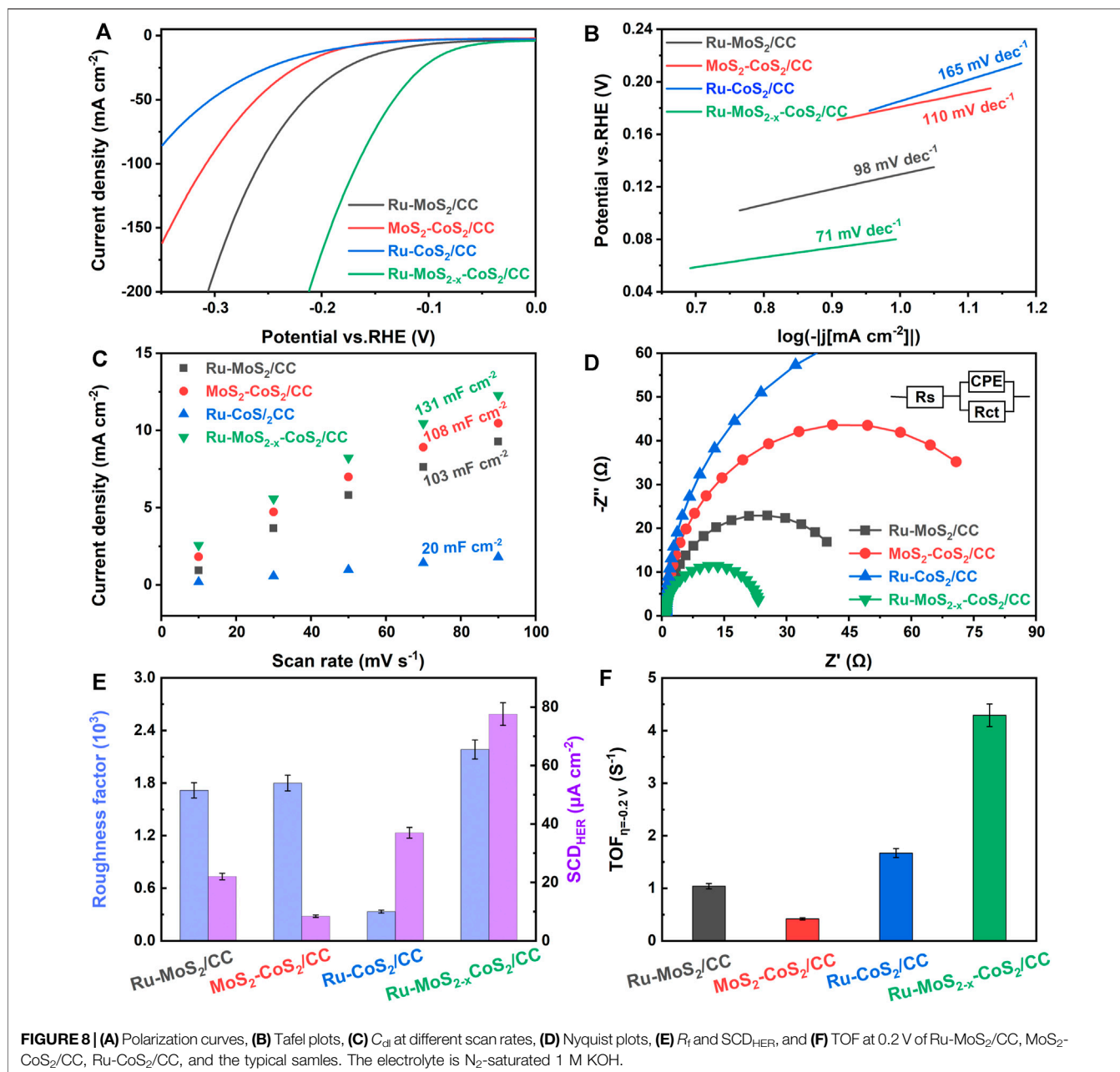
Additionally, **Figure 6** also demonstrates the influence of compositing with CoS$_2$ on $C_{S-vacancy}$ of the as-synthesized samples without Ru dopants. **Figure 6C** shows XRD patterns of MoS$_2$-CoS$_2$/CC-80, MoS$_2$-CoS$_2$/CC-240, MoS$_2$-CoS$_2$/CC-280, and MoS$_2$-CoS$_2$/CC-320. The influences of m_{Co} on intensities of the related peaks and RC of MoS$_2$ and CoS$_2$ are shown in **Figure 6C** and **Supplementary Figure S12**, suggesting a decline in the crystallinity of MoS$_2$ and an increase in crystallinity of CoS$_2$ as well. The trend in the variation of atom ratios of Co to (Co + Mo) of the as-synthesized samples without Ru dopants is the same as that of Ru-doped samples in **Figure 6D**, which implies the formation of more CoS$_2$ and richer heterojunctions at higher m_{Co}. Similarly, the more heterojunctions are, the stronger electron injection effect from CoS$_2$ to MoS$_{2-x}$ is obtained. For instance, Mo 3 day peaks of MoS$_2$-CoS$_2$/CC-240 display a negative shift of 0.15 eV in comparison with those of MoS$_2$-CoS$_2$/CC-80 from **Supplementary Figure S13**. At m_{Co} increasing to 320 mg, Mo 3 day peaks of MoS$_2$-CoS$_2$/CC-320 present a negative shift of about 0.36 eV compared to those of MoS$_2$-CoS$_2$/CC-80 (**Supplementary Figure S13**). Therefore, the atom ratios of S to Mo for these samples without Ru dopants also decrease with increasing m_{Co} (**Supplementary Table S3**), leading to an increase in $C_{S-vacancy}$ (**Figure 6E**) as well. Therefore, $C_{S-vacancy}$ of the

basal planes of Ru-MoS$_{2-x}$ can be efficiently regulated by simply changing m_{Co} based on the effect of electron injection from Ru-CoS$_2$ to Ru-MoS$_{2-x}$.

Together, either doping Ru or compositing with CoS$_2$ only regulates $C_{S-vacancy}$ of the as-synthesized samples within a narrow range, such as between 2.1 and 10.5% for doping Ru (**Figure 3E**) and 4.5 and 11.5% for compositing with CoS$_2$ (**Figure 6E**). Interestingly, synergistically regulating $C_{S-vacancy}$ of the as-synthesized samples, from 2.1 to 27.5% (**Figure 6E**), is realized by a new one-step doping-assisted compositing strategy.

HER Activities of Ru-MoS$_{2-X}$-CoS$_2$/CC Samples Synthesized at Various V

To find out the relationship between the microstructure and HER activity, we carefully investigate a series of electrochemical performances of Ru-MoS$_{2-x}$-CoS$_2$/CC samples synthesized at various V under the fixed m_{Co} (160 mg) in **Figures 7, 8**. According to **Figures 7A–D**, the typical samples exhibit the highest HER activity among these samples, such as an overpotential of about 170 mV at a current density of 100 mA cm^{-2} and a Tafel plot of 71 mV dec^{-1} in alkaline environments (1 M KOH), implying that low or excessive Ru dopant is disadvantageous for the HER activity of Ru-MoS$_{2-x}$-CoS$_2$/CC samples.

FIGURE 8 | (A) Polarization curves, **(B)** Tafel plots, **(C)** C_{dl} at different scan rates, **(D)** Nyquist plots, **(E)** R_f and SCD$_{HER}$, and **(F)** TOF at 0.2 V of Ru-MoS$_2$/CC, MoS$_2$-CoS$_2$/CC, Ru-CoS$_2$/CC, and the typical samles. The electrolyte is N$_2$-saturated 1 M KOH.

Figure 7C displays double-layer capacitance (C_{dl}) to evaluate electrochemical active surface area (ECSA), which is calculated by cyclic voltammetry (CV) curves in **Supplementary S14, 15**. From **Figure 7C** and **Figure 8C**, the typical samples also demonstrate the highest C_{dl} among all Ru-MoS$_{2-x}$-CoS$_2$/CC samples, reaching up to *ca.* 131 mF cm^{-2}. For 2H-MoS$_2$, its active sites are mainly from unsaturated sulfur atoms (Kibsgaard et al., 2012; Xie et al., 2013a; Liu et al., 2018). This is because the adsorption free energy of hydrogen atom (ΔG_H) of unsaturated sulfur atoms approaches zero (about -0.06 eV), which indicates their excellent H* adsorption–desorption property (Hinnemann et al., 2005). More recently, modulating sulfur vacancy into MoS$_2$-based materials has been developed as an efficient strategy (Tsai

et al., 2017; Park et al., 2018; Li Y. et al., 2021) to activate inert basal planes because EMAs can be tailored into newborn active sites (Wang X. et al., 2020). Therefore, the active sites of these Ru-MoS$_{2-x}$-CoS$_2$/CC samples should include unsaturated sulfur atoms and EMAs.

To confirm the difference in active sites for such Ru-MoS$_{2-x}$-CoS$_2$/CC samples, the inset of **Figure 7C** further shows the concentration of unsaturated sulfur atoms (USAs) of all samples based on XPS data from **Supplementary Figure S16**. From this inset, there is no significant difference in the concentration of USAs (C_{USAs}) for these samples. This may be closely related to preferentially exposed sulfur-edge atoms of Ru-MoS$_{2-x}$ nanosheet array vertically assembled on CC. At the same

time, this inset implies that USAs are not the essential factor for the most abundant active sites of the typical samples. From **Figure 3E**, $C_{\text{S-vacancy}}$ for Ru-MoS$_{2-x}$-CoS$_2$/CC-1.0, the typical samples, Ru-MoS$_{2-x}$-CoS$_2$/CC-7.0, Ru-MoS$_{2-x}$-CoS$_2$/CC-10.0, and Ru-MoS$_{2-x}$-CoS$_2$/CC-30.0 are 7.9, 17.1, 14.0, 12.5, and 12.0%, respectively. It is seen that $C_{\text{S-vacancy}}$ of the typical samples is higher than that of other Ru-MoS$_{2-x}$-CoS$_2$/CC samples. Consequently, we can reasonably conclude that the difference in active sites of RCM/CC should be dependent on $C_{\text{S-vacancy}}$. The formation of one S-vacancy means the occurrence of three EMAs at $C_{\text{S-vacancy}} < 18\%$ (Li et al., 2016a) because S-vacancy uniformly distributes on the basal planes of 2H-MoS$_{2-x}$. Obviously, under this situation, the higher $C_{\text{S-vacancy}}$ is obtained, the more EMAs or active sites are achieved. At m_{Co} = 160 mg, Ru doping firstly favors heterogeneous nucleation and growth of CoS$_2$ (**Figures 4C, I**) besides introducing a certain quantity S-vacancy into the basal planes. For instance, at V increasing to 4.0 ml, the typical samples demonstrate higher $C_{\text{S-vacancy}}$ (**Figure 3E**) than Ru-MoS$_{2-x}$-CoS$_2$/CC-1.0, maybe due to more heterogeneous interfaces between Ru-CoS$_2$ and Ru-MoS$_{2-x}$. Nevertheless, further increasing V hinders the formation of Ru-CoS$_2$ (**Figures 4F, I**) and leads to a decline in $C_{\text{S-vacancy}}$. Lower $C_{\text{S-vacancy}}$ could originate from fewer Schottky heterojunctions and a weaker electron injection effect of Ru-CoS$_2$ at excessively high V.

As another key factor for HER, the R_{CT} of all Ru-MoS$_{2-x}$-CoS$_2$/CC samples is investigated in **Figure 7D** and **Figure 8D**. These figures exhibit their Nyquist plots. Each semicircle represents the R_{CT} of the cathode reaction. The charge transfer of Ru-MoS$_{2-x}$-CoS$_2$/CC-1.0 or Ru-MoS$_{2-x}$-CoS$_2$/CC-7.0 is inferior to that of the typical samples. Moreover, further increasing V results in considerably unsatisfactory R_{CT} from **Figure 7D**. In our viewpoint, rich active sites will promote the occurrence of HER reaction in the cathode, implying efficient charge transfer for the typical samples. On the other hand, compositing with the metallic phase for fast electrode kinetics (He et al., 2020; Li et al., 2020; Zhou G. et al., 2021), such as CoS$_2$ (Li et al., 2020), carbon nanotube (Huang et al., 2017), and reduced graphene oxide (Wang Y. et al., 2020), is one of the important approaches to improving electrocatalytic HER activity. From **Figure 7D** and **Figure 8D**, Ru-MoS$_{2-x}$-CoS$_2$/CC-1.0 demonstrate better charge transfer compared to Ru-MoS$_{2-x}$/CC. Furthermore, the influence of V on R_{CT} is coincident with the trend in the variation of RC of Ru-CoS$_2$ (**Figure 3C**) and atom ratios of Co to (Co + Mo) (inset of **Figure 3A**) of all Ru-MoS$_{2-x}$-CoS$_2$/CC samples. Therefore, the higher crystallinity of cobalt disulfide or the more CoS$_2$ is obtained, the lower R_{CT} of the as-synthesized samples is achieved.

HER Activities of Ru-MoS$_{2-X}$-CoS$_2$/CC Samples Synthesized at Various m_{Co}

We further investigate the HER activity of Ru-MoS$_{2-x}$-CoS$_2$/CC samples synthesized at various m_{Co} under the fixed V (4.0 ml) in **Supplementary Figure S17**. From **Supplementary Figures S17A, B**, HER activities of Ru-MoS$_{2-x}$-CoS$_2$/CC-80 are an overpotential of about 228 mV at a current density of 100 mA cm^{-2} and a Tafel plot of 102 mV dec^{-1}. At m_{Co}

TABLE 1 | Comparison of the HER electrocatalytic activity of Ru-MoS$_{2-x}$-CoS$_2$/CC with some MoS$_2$-based HER electrocatalysts recently reported.

Samples	η_{10} (mV)	Ref
Co$_3$S$_4$/MoS$_2$ NRs	−166	Li et al. (2022b)
MoS$_2$@CoSe$_2$-CC	−101	Yuan et al. (2022)
NiS$_2$/MoS$_2$@GNS	−130	Balaji et al. (2022)
N-doped MoS$_2$/Ti$_3$C$_2$T$_x$	−80	Liu et al. (2021)
Co-E$_x$-MoS$_2$	−89	Luo et al. (2018)
SA-Ru-MoS$_2$	−76	Zhang et al. (2019a)
0.2NM (Ni(OH)$_2$/MoS$_2$)	−227	Zhao et al. (2018)
Co$_9$S$_8$-MoS$_2$@3DC	−177	Diao et al. (2019)
Ru-MoS$_2$	−98	Geng et al. (2022)
ZnS@C@MoS$_2$	−118	Liu et al. (2019)
Ru-MoS$_{2-x}$-CoS$_2$/CC	−73	This work

increasing to 160 mg, the typical samples demonstrate higher HER activity than other samples (**Figure 8A**; **Supplementary Figure S17A**). Further increasing m_{Co} leads to unsatisfactory overpotential and sluggish electrode kinetics, yielding the related data of 264 and 123 mV dec^{-1} for Ru-MoS$_{2-x}$-CoS$_2$/CC-240, 294 and 130 mV dec^{-1} for Ru-MoS$_{2-x}$-CoS$_2$/CC-280, and 301 and 140 mV dec^{-1} for Ru-MoS$_{2-x}$-CoS$_2$/CC-320 at the same current density.

To illustrate the reason why excessive m_{Co} is disadvantageous for HER activity, C_{dl} and C_{USAs} of all samples are tested in **Supplementary FIgure S17C** and **Supplementary Figure S18**, respectively. The corresponding CV curves related to **Supplementary FIgure S17C** are shown in **Supplementary Figure S19**. From **Supplementary FIgure S17C**, C_{dl} gradually increases with an increase in m_{Co}. For example, Ru-MoS$_{2-x}$-CoS$_2$/CC-80 display low C_{dl} (about 118 mF cm^{-2}) at m_{Co} = 80 mg. At m_{Co} increasing to 320 mg, the C_{dl} of Ru-MoS$_{2-x}$-CoS$_2$/CC-320 is as high as 199 mF cm^{-2}. We rationally hypothesize that this is closely related to $C_{\text{S-vacancy}}$, due to the fact that high $C_{\text{S-vacancy}}$ favors abundant EMAs. As we know, the basal planes in 2H-MoS$_2$ are inert, owing to ΔG_H reaching 2.1 eV (Zhou W. et al., 2021). Impressively, inert basal planes can be efficiently activated by a low concentration of S-vacancy (ca 4%) modulating into them because the corresponding ΔG_H closes to zero (Wang X. et al., 2020). It is not difficult to understand that such EMAs should be highly active, but the number is considerably poor.

According to the related literature (Wang X. et al., 2020), ΔG_H negatively shifts with an increase in $C_{\text{S-vacancy}}$, implying that hydrogen atoms do not easily desorb at excessive $C_{\text{S-vacancy}}$. For instance, at excessive m_{Co}, $C_{\text{S-vacancy}}$ of Ru-MoS$_{2-x}$-CoS$_2$/CC-320 reaches up to 27.5%. As expected, EMAs are abundant in this case, but the catalytic sites are of low activity, owing to the undesirable ΔG_H (Wang X. et al., 2020). Subsequently, a balance between the intrinsic activity and the number of EMAs to boost highly active EMAs could be realized by precisely regulating $C_{\text{S-vacancy}}$ to 17.1% (Wang X. et al., 2020). Consequently, the typical samples demonstrate the optimal HER activity among all samples. Furthermore, C_{USAs} of all samples except for Ru-MoS$_{2-x}$-CoS$_2$/CC-320 is almost the same as that of the typical samples. C_{USAs} of Ru-MoS$_{2-x}$-CoS$_2$/CC-320 (about 33.9%) is lower than that of other samples, which is responsible for the incompact Ru-MoS$_{2-x}$ shells (**Supplementary Figure S11D**), and the significant

decrease in the content of molybdenum disulfide (**Figure 6D**). This indicates that sulfur-edge atoms of $Ru-MoS_{2-x}$ nanosheets are not easy to be preferentially exposed for such samples synthesized at excessive m_{Co}.

Last but not least, **Supplementary Figure S17D** and **Figure 8D** further exhibit R_{CT} of all samples. Higher m_{Co} leads to higher R_{CT} of the related samples (**Supplementary Figure S17D**). For example, at m_{Co} reaching up to 320 mg, $Ru-MoS_{2-x}-CoS_2/CC$-320 display the highest R_{CT} among all $Ru-MoS_{2-x}-CoS_2/CC$ samples. It can be ascribed to insufficient highly active EMAs regardless of the higher RC of $Ru-CoS_2$ (**Figure 6A**; **Supplementary Figure S10**) for these samples synthesized at higher m_{Co}. Insufficient active sites could not promote redox half-reaction, thereby leading to inefficient charge transfer.

Comparison of HER Activities of the Typical Samples and Other Similar Electrocatalysts

HER activities of $Ru-MoS_2/CC$, MoS_2-CoS_2/CC, $Ru-CoS_2/CC$, and the typical samples are shown in **Figure 8A**. $Ru-CoS_2/CC$ display the lowest HER activity among these samples, suggesting that the activity of the typical samples is mainly from $Ru-MoS_{2-x}$ rather than $Ru-CoS_2$. In addition, $Ru-MoS_2/CC$ exhibit faster electrode kinetics than MoS_2-CoS_2/CC according to **Figure 8B**. In our viewpoint, the Ru-doped sites can significantly accelerate the sluggish water dissociation in alkaline HER (Li J. et al., 2021).

From **Figure 8C**, C_{dl} of $Ru-MoS_2/CC$ is only 103 mF cm^{-2} and lower than that of the typical samples. Furthermore, C_{USAs} of $Ru-MoS_2/CC$ (about 39.3%) is almost the same as that of the typical samples from **Supplementary Figure S18**. Therefore, the difference in active sites between $Ru-MoS_2/CC$ and the typical samples should be closely related to $C_{S-vacancy}$. Higher $C_{S-vacancy}$ indicates more highly active EMAs. As shown in **Figure 3E**, $C_{S-vacancy}$ of $Ru-MoS_2/CC$ is only about 3.1% by doping Ru, implying insufficient active sites. In our strategy, doping Ru coupled to compositing with CoS_2 synergistically regulates $C_{S-vacancy}$ of the as-synthesized samples from 2.1 to 27.5%. For instance, $C_{S-vacancy}$ of the typical samples reaches up to 17.1% (**Figure 3E**), which implies that rich highly active sites are successfully introduced into the typical samples. In terms of **Figure 8D**, R_{CT} of the typical samples is lower than that of $Ru-MoS_2/CC$. Besides rich active sites promoting redox half-reaction, high crystallized $Ru-CoS_2$ of the typical samples is another important factor to realize the efficient charge transfer during electrocatalysis. Next, the specific activity and turnover frequency (TOF) are further conducted to investigate the intrinsic activity of all samples (**Figures 8E, F**). C_{dl} of an ideal plane electrode is considered as 60 µF cm^{-2} (Levine and Smith, 1971); the roughness factor (R_f) can be calculated by the formula: $R_f = (C_{dl} \, 60^{-1}) \times 10^{+3}$. The specific alkaline HER current density (SCD_{HER}) is determined by the formula: $SCD_{HER} = j \, R_f^{-1}$ (Jovic et al., 2015; Jovic et al., 2016), where j is the current density at an overpotential of -0.2 V. From **Figure 8E**, the typical samples have not only the largest R_f ($2.18 \times 10^{+3}$) but also the highest specific activity (about 77.6 µA cm^{-2}) among all samples. In addition, the TOF for these samples is obtained by the formula TOF = $jS \, (2nF)^{-1}$. Here, S is the geometrical surface area in cm^2

and F is the Faraday constant. The value of n is the number of active sites (mol), which is confirmed according to the previously reported literature (Tian et al., 2014). The typical samples also exhibit the highest intrinsic activity among all samples, about 4.29 s^{-1} in **Figure 8F**. Moreover, the comparison between the typical samples and other similar electrocatalysts is provided in **Table 1**. The typical samples exhibit higher HER activity than other similar electrocatalysts listed in **Table 1**, which is ascribed to two factors: abundant active sites and accelerated electrode kinetics during the HER process.

The Long-Term Durability of the Typical Samples

In addition, LSV curves of the typical samples before and after 1000 cycles are recorded to evaluate their durability, and just a 10 mV negative shift at a current density of -100 mA cm^{-2} is seen in **Supplementary Figure S20A, B**; the chronoamperometric response (i ~ t) of the typical samples displays negligible attenuation of the current density for 10 h. Moreover, no significant change is observed in the morphology and phase structure after 1000 cycles (**Supplementary Figures S21, 22**). All results suggest that the typical samples possess remarkable long-term durability for HER in alkaline media.

CONCLUSION

Herein, we develop a one-step Ru doping coupled to compositing with the CoS_2 strategy for the fabrication of $Ru-MoS_{2-x}-CoS_2/CC$. In our strategy, Ru doping is advantageous for the formation of S-vacancy in the basal planes of MoS_2. More importantly, Ru doping affects microstructures of CoS_2, which has a significant influence on $C_{S-vacancy}$ of $Ru-MoS_{2-x}$ nanosheets in $Ru-MoS_{2-x}-CoS_2/CC$ samples in turn. At the fixed m_{Co} (160 mg), Ru doping favors the heterogeneous nucleation and growth of CoS_2 at V increasing to 4.0 ml, which leads to a high crystallinity of $Ru-CoS_2$ and rich heterogeneous interfaces between $Ru-CoS_2$ and $Ru-MoS_{2-x}$. This facilitates the electron transfer from $Ru-CoS_2$ to $Ru-MoS_{2-x}$, indicating an increase in $C_{S-vacancy}$, thereby increasing $C_{S-vacancy}$ of the MoS_2-based materials. However, further increasing V results in a low crystallinity of $Ru-CoS_2$ and poor heterojunctions, implying a weaker electron injection effect of $Ru-CoS_2$ and low $C_{S-vacancy}$. At fixed V (4.0 ml of $RuCl_3$ solution), the electron injection effect increases gradually with the increase in m_{Co}, which means more S^{2-} escaping from $Ru-MoS_2$ nanosheets at higher m_{Co}. Therefore, synergistically regulating $C_{S-vacancy}$ of the as-synthesized samples, from 2.1 to 27.5%, is realized by a new one-step Ru doping coupled to compositing with the CoS_2 strategy. High $C_{S-vacancy}$ indicates abundant EMAs. Impressively, inert basal planes can be efficiently activated by modulating low $C_{S-vacancy}$ into $Ru-MoS_{2-x}-CoS_2/CC$ samples. However, the number is considerably poor. Additionally, hydrogen atoms do not easily desorb at excessive $C_{S-vacancy}$. This is because EMAs are abundant in this case, but the catalytic sites are of low activity, owing to the undesirable ΔG_H. By precisely regulating $C_{S-vacancy}$ to 17.1%, a balance

between the intrinsic activity and the number of EMAs to boost highly active EMAs should be realized. Consequently, the typical samples demonstrate the optimal alkaline HER activity among all samples, such as a low overpotential of 170 mV at 100 mA cm^{-2}, a large SCD$_{HER}$ of 77.6 μA cm^{-2}, and a TOF of 4.29 s^{-1} at - 0.2 V as well as excellent long-term stability. The results pave a new approach to activating inert basal planes in MoS$_2$ for efficient hydrogen evolution and promise important applications in the fields of electrocatalysis or energy conversion.

DATA AVAILABILITY STATEMENT

The original contributions presented in the study are included in the article/**Supplementary Material**; further inquiries can be directed to the corresponding authors.

AUTHOR CONTRIBUTIONS

X-YL has made substantial contributions to the design of this work and has drafted the work. S-JZ has made substantial contributions to the acquisition, analysis, and interpretation of data for the work. YW has revised the work critically for the important intellectual content and has approved the final version to be published. TL, X-YY, and C-FY have made some contributions to the analysis and interpretation of data for the work. YL has given some important suggestions for this revised article. BS has given some suggestions on preparing this article. L-HC has provided some important ideas for the design of this work and has approved the final version to be published.

SUPPLEMENTARY MATERIAL

The Supplementary Material for this article can be found online at: https://www.frontiersin.org/articles/10.3389/fchem.2022.915468/full#supplementary-material

REFERENCES

Balaji, D., Madhavan, J., Vinesh, V., Neppolian, B., AlSalhi, M. S., and Prasad, S. (2022). Graphene Supported Flower-like NiS2/MoS2 Mixed Phase Nano-Composites as a Low Cost Electrode Material for Hydrogen Evolution Reaction in Alkaline Media. *Mater. Chem. Phys.* 280, 125839. doi:10.1016/j.matchemphys.2022.125839

Chakraborty, I., Malik, P. K., and Moulik, S. P. (2006). Preparation and Characterisation of CoS2 Nanomaterial in Aqueous Cationic Surfactant Medium of Cetyltrimethylammonium Bromide (CTAB). *J. Nanopart. Res.* 8 (6), 889–897. doi:10.1007/s11051-005-9032-y

Chen, T.-T., Wang, R., Li, L.-K., Li, Z.-J., and Zang, S.-Q. (2020). MOF-derived Co9S8/MoS2 Embedded in Tri-doped Carbon Hybrids for Efficient Electrocatalytic Hydrogen Evolution. *J. Energy Chem.* 44, 90–96. doi:10.1016/j.jechem.2019.09.018

Deng, J., Li, H., Wang, S., Ding, D., Chen, M., Liu, C., et al. (2017). Multiscale Structural and Electronic Control of Molybdenum Disulfide Foam for Highly Efficient Hydrogen Production. *Nat. Commun.* 8 (1), 14430. doi:10.1038/ncomms14430

Diao, L., Zhang, B., Sun, Q., Wang, N., Zhao, N., Shi, C., et al. (2019). An In-Plane Co9S8@MoS2 Heterostructure for the Hydrogen Evolution Reaction in Alkaline Media. *Nanoscale* 11 (44), 21479–21486. doi:10.1039/C9NR06609H

Djara, R., Holade, Y., Merzouki, A., Lacour, M.-A., Masquelez, N., Flaud, V., et al. (2020). Nanostructured Carbon-Nitrogen-Sulfur-Nickel Networks Derived from Polyaniline as Bifunctional Catalysts for Water Splitting. *Front. Chem.* 8, 22. doi:10.3389/fchem.2020.00385

Feng, J.-X., Wu, J.-Q., Tong, Y.-X., and Li, G.-R. (2018). Efficient Hydrogen Evolution on Cu Nanodots-Decorated Ni3S2 Nanotubes by Optimizing Atomic Hydrogen Adsorption and Desorption. *J. Am. Chem. Soc.* 140 (2), 610–617. doi:10.1021/jacs.7b08521

Gan, X., Lee, L. Y. S., Wong, K.-y., Lo, T. W., Ho, K. H., Lei, D. Y., et al. (2018). 2H/1T Phase Transition of Multilayer MoS2 by Electrochemical Incorporation of S Vacancies. *ACS Appl. Energy Mat.* 1 (9), 4754–4765. doi:10.1021/acsaem.8b00875

Gao, B., Du, X., Li, Y., Ding, S., Xiao, C., and Song, Z. (2020). Deep Phase Transition of MoS2 for Excellent Hydrogen Evolution Reaction by a Facile C-Doping Strategy. *ACS Appl. Mat. Interfaces* 12 (1), 877–885. doi:10.1021/acsami.9b18940

Ge, R., Wang, Y., Li, Z., Xu, M., Xu, S. M., Zhou, H., et al. (2022). Selective Electrooxidation of Biomass-Derived Alcohols to Aldehydes in a Neutral Medium: Promoted Water Dissociation over a Nickel-Oxide-Supported Ruthenium Single-Atom Catalyst. *Angew. Chem. Int. Ed.* 61. doi:10.1002/anie.202200211

Geng, S., Tian, F., Li, M., Liu, Y., Sheng, J., Yang, W., et al. (2022). Activating Interfacial S Sites of MoS2 Boosts Hydrogen Evolution Electrocatalysis. *Nano Res.* 15 (3), 1809–1816. doi:10.1007/s12274-021-3755-7

Gong, F., Ye, S., Liu, M., Zhang, J., Gong, L., Zeng, G., et al. (2020). Boosting Electrochemical Oxygen Evolution over Yolk-Shell Structured O-MoS2 Nanoreactors with Sulfur Vacancy and Decorated Pt Nanoparticles. *Nano Energy* 78, 105284. doi:10.1016/j.nanoen.2020.105284

Hao, J., Yang, W., Peng, Z., Zhang, C., Huang, Z., and Shi, W. (2017). A Nitrogen Doping Method for CoS2 Electrocatalysts with Enhanced Water Oxidation Performance. *ACS Catal.* 7 (6), 4214–4220. doi:10.1021/acscatal.7b00792

He, S., Du, H., Wang, K., Liu, Q., Sun, J., Liu, Y., et al. (2020). Low-temperature Molten Salt Synthesis of MoS2@CoS2 Heterostructures for Efficient Hydrogen Evolution Reaction. *Chem. Commun.* 56 (41), 5548–5551. doi:10.1039/D0CC01726D

Hinnemann, B., Moses, P. G., Bonde, J., Jørgensen, K. P., Nielsen, J. H., Horch, S., et al. (2005). Biomimetic Hydrogen Evolution: MoS2 Nanoparticles as Catalyst for Hydrogen Evolution. *J. Am. Chem. Soc.* 127 (15), 5308–5309. doi:10.1021/ja0504690

Huang, H., Huang, W., Yang, Z., Huang, J., Lin, J., Liu, W., et al. (2017). Strongly Coupled MoS2 Nanoflake-Carbon Nanotube Nanocomposite as an Excellent Electrocatalyst for Hydrogen Evolution Reaction. *J. Mat. Chem. A* 5 (4), 1558–1566. doi:10.1039/C6TA09612C

Huang, J., Hou, D., Zhou, Y., Zhou, W., Li, G., Tang, Z., et al. (2015). MoS2 Nanosheet-Coated CoS2 Nanowire Arrays on Carbon Cloth as Three-Dimensional Electrodes for Efficient Electrocatalytic Hydrogen Evolution. *J. Mat. Chem. A* 3 (45), 22886–22891. doi:10.1039/C5TA07234D

Huang, N., Ding, Y., Yan, S., Yang, L., Sun, P., Huang, C., et al. (2019). Ultrathin MoS2 Nanosheets Vertically Grown on CoS2 Acicular Nanorod Arrays: A Synergistic Three-Dimensional Shell/Core Heterostructure for High-Efficiency Hydrogen Evolution at Full pH. *ACS Appl. Energy Mat.* 2 (9), 6751–6760. doi:10.1021/acsaem.9b01219

Jiang, J., Cong, H., Huang, X., Sun, R., Li, Y., Xu, W., et al. (2022). Three-dimensional ZnCo/MoS2-Co3S4/NF Heterostructure Supported on Nickel Foam as Highly Efficient Catalyst for Hydrogen Evolution Reaction. *Int. J. Hydrogen Energy* 47 (5), 2947–2957. doi:10.1016/j.ijhydene.2021.10.217

Jing, Y., Lei, Q., Hu, G., He, J., Lei, X., Wang, F., et al. (2020). PVP/ZIF-8-derived Zn, Ni Co-loaded N-Doped Porous Carbon as a Catalyst for an Efficient Hydrogen Evolution Reaction. *Front. Chem.* 8, 6. doi:10.3389/fchem.2020.00723

Jović, B. M., Jović, V. D., Lačnjevac, U. Č., Gajić-Krstajić, L., and Krstajić, N. V. (2015). Ni-(Ebonex-supported Ir) Composite Coatings as Electrocatalysts for Alkaline Water Electrolysis. Part I: Hydrogen Evolution. *Int. J. Hydrogen Energy* 40 (33), 10480–10490. doi:10.1016/j.ijhydene.2015.06.127

Jović, B. M., Jović, V. D., Lačnjevac, U. Č., Stevanović, S. I., Kovač, J., Radović, M., et al. (2016). Ru Layers Electrodeposited onto Highly Stable Ti2AlC Substrates as Cathodes for Hydrogen Evolution in Sulfuric Acid Solutions. *J. Electroanal. Chem.* 766, 78–86. doi:10.1016/j.jelechem.2016.01.038

Kang, Y. (2021). Interplay between Transition-Metal Dopants and Sulfur Vacancies in MoS2 Electrocatalyst. *Surf. Sci.* 704, 121759. doi:10.1016/j.susc.2020.121759

Kibsgaard, J., Chen, Z., Reinecke, B. N., and Jaramillo, T. F. (2012). Engineering the Surface Structure of MoS2 to Preferentially Expose Active Edge Sites for Electrocatalysis. *Nat. Mater* 11 (11), 963–969. doi:10.1038/nmat3439

Levine, S., and Smith, A. L. (1971). Theory of the Differential Capacity of the Oxide/aqueous Electrolyte Interface. *Discuss. Faraday Soc.* 52 (0), 290–301. doi:10.1039/DF9715200290

Li, C., Liu, Y., Zhuo, Z., Ju, H., Li, D., Guo, Y., et al. (2018). Local Charge Distribution Engineered by Schottky Heterojunctions toward Urea Electrolysis. *Adv. Energy Mat.* 8 (27), 1801775. doi:10.1002/aenm.201801775

Li, H., Tsai, C., Koh, A. L., Cai, L., Contryman, A. W., Fragapane, A. H., et al. (2016a). Activating and Optimizing MoS2 Basal Planes for Hydrogen Evolution through the Formation of Strained Sulphur Vacancies. *Nat. Mater* 15 (1), 48–53. doi:10.1038/nmat4465

Li, H., Tsai, C., Koh, A. L., Cai, L., Contryman, A. W., Fragapane, A. H., et al. (2016b). Erratum: Corrigendum: Activating and Optimizing MoS2 Basal Planes for Hydrogen Evolution through the Formation of Strained Sulphur Vacancies. *Nat. Mater* 15 (3), 364. doi:10.1038/nmat4564

Li, J., Li, Y., Wang, J., Zhang, C., Ma, H., Zhu, C., et al. (2022a). Elucidating the Critical Role of Ruthenium Single Atom Sites in Water Dissociation and Dehydrogenation Behaviors for Robust Hydrazine Oxidation-Boosted Alkaline Hydrogen Evolution. *Adv. Funct. Mater.* 32, 2109439. doi:10.1002/adfm.202109439

Li, J., Zhang, C., Ma, H., Wang, T., Guo, Z., Yang, Y., et al. (2021a). Modulating Interfacial Charge Distribution of Single Atoms Confined in Molybdenum Phosphosulfide Heterostructures for High Efficiency Hydrogen Evolution. *Chem. Eng. J.* 414, 128834. doi:10.1016/j.cej.2021.128834

Li, L., Qin, Z., Ries, L., Hong, S., Michel, T., Yang, J., et al. (2019). Role of Sulfur Vacancies and Undercoordinated Mo Regions in MoS2 Nanosheets toward the Evolution of Hydrogen. *ACS Nano* 13 (6), 6824–6834. doi:10.1021/acsnano.9b01583

Li, S., Sirisomboonchai, S., An, X., Ma, X., Li, P., Ling, L., et al. (2020). Engineering Interfacial Structures to Accelerate Hydrogen Evolution Efficiency of MoS2 over a Wide pH Range. *Nanoscale* 12 (12), 6810–6820. doi:10.1039/D0NR00008F

Li, Y., Wang, H., Xie, L., Liang, Y., Hong, G., and Dai, H. (2011). MoS2 Nanoparticles Grown on Graphene: An Advanced Catalyst for the Hydrogen Evolution Reaction. *J. Am. Chem. Soc.* 133 (19), 7296–7299. doi:10.1021/ja201269b

Li, Y., Zuo, S., Li, Q.-H., Wu, X., Zhang, J., Zhang, H., et al. (2021b). Vertically Aligned MoS2 with In-Plane Selectively Cleaved Mo-S Bond for Hydrogen Production. *Nano Lett.* 21 (4), 1848–1855. doi:10.1021/acs.nanolett.0c04978

Li, Z., Xu, W., Yu, X., Yang, S., Zhou, Y., Zhou, K., et al. (2022b). Synergistic Effect between 1D Co3S4/MoS2 Heterostructures to Boost the Performance for Alkaline Overall Water Splitting. *Inorg. Chem. Front.* 9, 2139–2149. doi:10.1039/D1QI01646F

Lin, H., Li, H., Li, Y., Liu, J., Wang, X., and Wang, L. (2017). Hierarchical CoS/MoS2 and Co3S4/MoS2/Ni2P Nanotubes for Efficient Electrocatalytic Hydrogen Evolution in Alkaline Media. *J. Mat. Chem. A* 5 (48), 25410–25419. doi:10.1039/C7TA08760H

Lin, J., Wang, P., Wang, H., Li, C., Si, X., Qi, J., et al. (2019). Defect-Rich Heterogeneous MoS 2/NiS 2 Nanosheets Electrocatalysts for Efficient Overall Water Splitting. *Adv. Sci.* 6 (14), 1900246. doi:10.1002/advs.201900246

Liu, D., Lv, Z., Dang, J., Ma, W., Jian, K., Wang, M., et al. (2021). Nitrogen-Doped MoS2/Ti3C2TX Heterostructures as Ultra-efficient Alkaline HER Electrocatalysts. *Inorg. Chem.* 60 (13), 9932–9940. doi:10.1021/acs.inorgchem.1c01193

Liu, G., Robertson, A. W., Li, M. M.-J., Kuo, W. C. H., Darby, M. T., Muhieddine, M. H., et al. (2017). MoS2 Monolayer Catalyst Doped with Isolated Co Atoms for the Hydrodeoxygenation Reaction. *Nat. Chem.* 9 (8), 810–816. doi:10.1038/nchem.2740

Liu, L., Wang, Y., Zhao, Y., Wang, Y., Zhang, Z., Wu, T., et al. (2022a). Ultrahigh Pt-Mass-Activity Hydrogen Evolution Catalyst Electrodeposited from Bulk Pt. *Adv. Funct. Mater.* 32 (20), 2112207. doi:10.1002/adfm.202112207

Liu, S., Li, S., Sekar, K., Li, R., Zhu, Y., Xing, R., et al. (2019). Hierarchical ZnS@C@MoS2 Core-Shell Nanostructures as Efficient Hydrogen Evolution Electrocatalyst for Alkaline Water Electrolysis. *Int. J. Hydrogen Energy* 44 (47), 25310–25318. doi:10.1016/j.ijhydene.2019.08.048

Liu, W., Wang, X., Yu, H., and Yu, J. (2018). Direct Photoinduced Synthesis of Amorphous CoMoSx Cocatalyst and Its Improved Photocatalytic H2-Evolution Activity of CdS. *ACS Sustain. Chem. Eng.* 6 (9), 12436–12445. doi:10.1021/acssuschemeng.8b02971

Liu, X., Yin, Z., Cui, M., Gao, L., Liu, A., Su, W.-N., et al. (2022b). Double Shelled Hollow CoS2@MoS2@NiS2 Polyhedron as Advanced Trifunctional Electrocatalyst for Zinc-Air Battery and Self-Powered Overall Water Splitting. *J. Colloid Interface Sci.* 610, 653–662. doi:10.1016/j.jcis.2021.11.115

Luo, Y., Li, X., Cai, X., Zou, X., Kang, F., Cheng, H.-M., et al. (2018). Two-Dimensional MoS2 Confined Co(OH)2 Electrocatalysts for Hydrogen Evolution in Alkaline Electrolytes. *ACS Nano* 12 (5), 4565–4573. doi:10.1021/acsnano.8b00942

Luo, Z., Zhang, H., Yang, Y., Wang, X., Li, Y., Jin, Z., et al. (2020). Reactant Friendly Hydrogen Evolution Interface Based on Di-anionic MoS2 Surface. *Nat. Commun.* 11 (1), 1116. doi:10.1038/s41467-020-14980-z

Ma, Y., Hai, G., Atinafu, D. G., Dong, W., Li, R., Hou, C., et al. (2020). Carbon Inserted Defect-Rich MoS2−X nanosheets@CdSnanospheres for Efficient Photocatalytic Hydrogen Evolution under Visible Light Irradiation. *J. Colloid Interface Sci.* 569, 89–100. doi:10.1016/j.jcis.2020.02.071

Nguyen, D. C., Luyen Doan, T. L., Prabhakaran, S., Tran, D. T., Kim, D. H., Lee, J. H., et al. (2021). Hierarchical Co and Nb Dual-Doped MoS2 Nanosheets Shelled Micro-TiO2 Hollow Spheres as Effective Multifunctional Electrocatalysts for HER, OER, and ORR. *Nano Energy* 82, 105750. doi:10.1016/j.nanoen.2021.105750

Park, S., Park, J., Abroshan, H., Zhang, L., Kim, J. K., Zhang, J., et al. (2018). Enhancing Catalytic Activity of MoS2 Basal Plane S-Vacancy by Co Cluster Addition. *ACS Energy Lett.* 3 (11), 2685–2693. doi:10.1021/acsenergylett.8b01567

Qi, K., Cui, X., Gu, L., Yu, S., Fan, X., Luo, M., et al. (2019). Single-atom Cobalt Array Bound to Distorted 1T MoS2 with Ensemble Effect for Hydrogen Evolution Catalysis. *Nat. Commun.* 10 (1), 5231. doi:10.1038/s41467-019-12997-7

Smyth, D. M. (2000). The Effects of Dopants on the Properties of Metal Oxides. *Solid State Ion.* 129 (1), 5–12. doi:10.1016/S0167-2738(99)00312-4

Tian, J., Liu, Q., Asiri, A. M., and Sun, X. (2014). Self-Supported Nanoporous Cobalt Phosphide Nanowire Arrays: An Efficient 3D Hydrogen-Evolving

Cathode over the Wide Range of pH 0-14. *J. Am. Chem. Soc.* 136 (21), 7587–7590. doi:10.1021/ja503372r

Tsai, C., Li, H., Park, S., Park, J., Han, H. S., Nørskov, J. K., et al. (2017). Electrochemical Generation of Sulfur Vacancies in the Basal Plane of MoS2 for Hydrogen Evolution. *Nat. Commun.* 8 (1), 15113. doi:10.1038/ncomms15113

Venkateshwaran, S., and Senthil Kumar, S. M. (2019). Template-Driven Phase Selective Formation of Metallic 1T-MoS2 Nanoflowers for Hydrogen Evolution Reaction. *ACS Sustain. Chem. Eng.* 7 (2), 2008–2017. doi:10.1021/acssuschemeng.8b04335

Wang, D., Li, Q., Han, C., Xing, Z., and Yang, X. (2019a). Single-atom Ruthenium Based Catalyst for Enhanced Hydrogen Evolution. *Appl. Catal. B Environ.* 249, 91–97. doi:10.1016/j.apcatb.2019.02.059

Wang, F., Yu, H., Feng, T., Zhao, D., Piao, J., and Lei, J. (2020a). Surface Roughed and Pt-Rich Bimetallic Electrocatalysts for Hydrogen Evolution Reaction. *Front. Chem.* 8, 9. doi:10.3389/fchem.2020.00422

Wang, H., Tsai, C., Kong, D., Chan, K., Abild-Pedersen, F., Nørskov, J. K., et al. (2015). Transition-metal Doped Edge Sites in Vertically Aligned MoS2 Catalysts for Enhanced Hydrogen Evolution. *Nano Res.* 8 (2), 566–575. doi:10.1007/s12274-014-0677-7

Wang, J., Bo, T., Shao, B., Zhang, Y., Jia, L., Tan, X., et al. (2021a). Effect of S Vacancy in Cu3SnS4 on High Selectivity and Activity of Photocatalytic CO2 Reduction. *Appl. Catal. B Environ.* 297, 120498. doi:10.1016/j.apcatb.2021.120498

Wang, R., Sun, P., Wang, H., and Wang, X. (2017). Pulsed Laser Deposition of Amorphous Molybdenum Disulfide Films for Efficient Hydrogen Evolution Reaction. *Electrochimica Acta* 258, 876–882. doi:10.1016/j.electacta.2017.11.138

Wang, X., Zhang, Y., Si, H., Zhang, Q., Wu, J., Gao, L., et al. (2020b). Single-Atom Vacancy Defect to Trigger High-Efficiency Hydrogen Evolution of MoS2. *J. Am. Chem. Soc.* 142 (9), 4298–4308. doi:10.1021/jacs.9b12113

Wang, Y.-l., Huang, Q., Sun, G.-q., Li, X.-y., Chen, L.-h., Su, B.-l., et al. (2021b). Synergistic Zinc Doping and Defect Engineering toward MoS2 Nanosheet Arrays for Highly Efficient Electrocatalytic Hydrogen Evolution. *Dalton Trans.* 50 (17), 5770–5775. doi:10.1039/D0DT04207B

Wang, Y.-l., Sun, G.-q., Chen, L.-h., Du, Z.-k., Li, X.-y., Ye, C.-f., et al. (2021c). Engineering Dual Defective Graphenes to Synergistically Improve Electrocatalytic Hydrogen Evolution. *Appl. Surf. Sci.* 566, 150712. doi:10.1016/j.apsusc.2021.150712

Wang, Y., Lu, F., Su, K., Zhang, N., Zhang, Y., Wang, M., et al. (2020c). Engineering Mo-O-C Interface in MoS2@rGO via Charge Transfer Boosts Hydrogen Evolution. *Chem. Eng. J.* 399, 126018. doi:10.1016/j.cej.2020.126018

Wang, Y., Qi, K., Yu, S., Jia, G., Cheng, Z., Zheng, L., et al. (2019b). Revealing the Intrinsic Peroxidase-Like Catalytic Mechanism of Heterogeneous Single-Atom Co-MoS2. *Nano-Micro Lett.* 11 (1), 102. doi:10.1007/s40820-019-0324-7

Xie, J., Zhang, H., Li, S., Wang, R., Sun, X., Zhou, M., et al. (2013a). Defect-Rich MoS2Ultrathin Nanosheets with Additional Active Edge Sites for Enhanced Electrocatalytic Hydrogen Evolution. *Adv. Mat.* 25 (40), 5807–5813. doi:10.1002/adma.201302685

Xie, J., Zhang, J., Li, S., Grote, F., Zhang, X., Zhang, H., et al. (2013b). Controllable Disorder Engineering in Oxygen-Incorporated MoS2 Ultrathin Nanosheets for Efficient Hydrogen Evolution. *J. Am. Chem. Soc.* 135 (47), 17881–17888. doi:10.1021/ja408329q

Xu, X., Shi, W., Li, P., Ye, S., Ye, C., Ye, H., et al. (2017). Facile Fabrication of Three-Dimensional Graphene and Metal-Organic Framework Composites and Their Derivatives for Flexible All-Solid-State Supercapacitors. *Chem. Mat.* 29 (14), 6058–6065. doi:10.1021/acs.chemmater.7b01947

Xu, Y., Wang, L., Liu, X., Zhang, S., Liu, C., Yan, D., et al. (2016). Monolayer MoS2with S Vacancies from Interlayer Spacing Expanded Counterparts for Highly Efficient Electrochemical Hydrogen Production. *J. Mat. Chem. A* 4 (42), 16524–16530. doi:10.1039/C6TA06534A

Yan, Y., Huang, J., Wang, X., Gao, T., Zhang, Y., Yao, T., et al. (2018). Ruthenium Incorporated Cobalt Phosphide Nanocubes Derived from a Prussian Blue Analog for Enhanced Hydrogen Evolution. *Front. Chem.* 6, 8. doi:10.3389/fchem.2018.00521

Yao, N., Li, P., Zhou, Z., Meng, R., Cheng, G., and Luo, W. (2019). Nitrogen Engineering on 3D Dandelion-Flower-Like CoS 2 for High-Performance Overall Water Splitting. *Small* 15 (31), 1901993. doi:10.1002/smll.201901993

Yin, H., Zhao, S., Zhao, K., Muqsit, A., Tang, H., Chang, L., et al. (2015). Ultrathin Platinum Nanowires Grown on Single-Layered Nickel Hydroxide with High Hydrogen Evolution Activity. *Nat. Commun.* 6 (1), 6430. doi:10.1038/ncomms7430

Yu, H., Yu, X., Chen, Y., Zhang, S., Gao, P., and Li, C. (2015). A Strategy to Synergistically Increase the Number of Active Edge Sites and the Conductivity of MoS2 Nanosheets for Hydrogen Evolution. *Nanoscale* 7 (19), 8731–8738. doi:10.1039/C5NR00670H

Yuan, L., Zhang, Y., Chen, J., Li, Y., Ren, X., Zhang, P., et al. (2022). MoS2 Nanosheets Vertically Grown on CoSe2 Hollow Nanotube Arrays as an Efficient Catalyst for the Hydrogen Evolution Reaction. *Nanoscale* 14 (6), 2490–2501. doi:10.1039/D1NR05941F

Zhang, J., Xu, X., Yang, L., Cheng, D., and Cao, D. (2019a). Single-Atom Ru Doping Induced Phase Transition of MoS 2 and S Vacancy for Hydrogen Evolution Reaction. *Small Methods* 3 (12), 1900653. doi:10.1002/smtd.201900653

Zhang, X., Zhou, F., Zhang, S., Liang, Y., and Wang, R. (2019b). Engineering MoS 2 Basal Planes for Hydrogen Evolution via Synergistic Ruthenium Doping and Nanocarbon Hybridization. *Adv. Sci.* 6 (10), 1900090. doi:10.1002/advs.201900090

Zhao, G., Lin, Y., Rui, K., Zhou, Q., Chen, Y., Dou, S. X., et al. (2018). Epitaxial Growth of Ni(OH)2 Nanoclusters on MoS2 Nanosheets for Enhanced Alkaline Hydrogen Evolution Reaction. *Nanoscale* 10 (40), 19074–19081. doi:10.1039/C8NR07045H

Zhou, G., Wu, X., Zhao, M., Pang, H., Xu, L., Yang, J., et al. (2021a). Interfacial Engineering-Triggered Bifunctionality of CoS 2/MoS 2 Nanocubes/Nanosheet Arrays for High-Efficiency Overall Water Splitting. *ChemSusChem* 14 (2), 699–708. doi:10.1002/cssc.202002338

Zhou, W., Dong, L., Tan, L., and Tang, Q. (2021b). First-principles Study of Sulfur Vacancy Concentration Effect on the Electronic Structures and Hydrogen Evolution Reaction of MoS2. *Nanotechnology* 32 (14), 145718. doi:10.1088/1361-6528/abd49f

Zhu, Y., Song, L., Song, N., Li, M., Wang, C., and Lu, X. (2019). Bifunctional and Efficient CoS2-C@MoS2 Core-Shell Nanofiber Electrocatalyst for Water Splitting. *ACS Sustain. Chem. Eng.* 7 (3), 2899–2905. doi:10.1021/acssuschemeng.8b05462